

1 **Barium isotopes in mid-ocean ridge hydrothermal vent**
2 **fluids: a source of isotopically heavy Ba to the ocean**

3

4

5

6 **Yu-Te Hsieh^{a,*}, Luke Bridgestock^a, Peter P. Scheuermann^b, William E. Seyfried**
7 **Jr^b., and Gideon M. Henderson^a**

8

9

10 ^a**Department of Earth Sciences, University of Oxford, UK**

11 ^b**Department of Earth and Environmental Sciences, University of Minnesota,**
12 **USA**

13

14 **Keywords:** Ba isotopes; mid-ocean ridge; hydrothermal; barite; isotopic fractionation.

15 **Highlights:**

16 1. MOR vent fluids show the largest range of $\delta^{138/134}\text{Ba}$ seen so far in marine systems.

17 2. Endmember vent fluid $\delta^{138/134}\text{Ba}$ values are the same as those of the source rocks.

18 3. Barite precipitation leads to high $\delta^{138/134}\text{Ba}$ values in vent fluids as they evolve.

19 4. Hydrothermal Ba input may explain non-conservative $\delta^{138/134}\text{Ba}$ seen in deep
20 waters.

21 5. Hydrothermal input contributes 3-9% of the Ba in some Atlantic deep waters.

22

23 **Accepted manuscript for publication in *Geochimica et Cosmochimica Acta***

24 <https://doi.org/10.1016/j.gca.2020.09.037>

25 ***Corresponding author: yu-te.hsieh@earth.ox.ac.uk**

26 **Abstract**

27 Mid-ocean ridge (MOR) hydrothermal vent fluids are enriched with dissolved
28 barium, but due to barite (BaSO_4) precipitation during mixing between Ba-bearing vent
29 fluids and SO_4 -bearing seawater, the magnitude of hydrothermal Ba input to the ocean
30 remains uncertain. Deep-ocean Ba isotopes show evidence for non-conservative
31 behavior, which might be explained by input of isotopically heavy hydrothermal Ba. In
32 this study we present the first Ba isotope data in mid-ocean ridge hydrothermal vent
33 fluids and particles from systems on the Mid-Atlantic Ridge (Rainbow 36°N and TAG
34 26°N), the East Pacific Rise (EPR9-10°N and 13°N) and the Juan de Fuca Ridge (MEF
35 and ASHES). The vent fluids display a wide range of dissolved Ba concentrations from
36 0.43 to 97.9 $\mu\text{mol/kg}$ and $\delta^{138/134}\text{Ba}$ values from -0.26 to +0.91 ‰, but are modified
37 relative to initial composition due to precipitation of barite. Calculated endmember vent
38 fluid $\delta^{138/134}\text{Ba}$ values, prior to barite precipitation, are between -0.17 and +0.09 ‰,
39 consistent with the values observed in oceanic basalts and pelagic sediments. Water-
40 rock interaction at depth in the oceanic crust appears to occur without Ba isotope
41 fractionation. During subsequent venting and mixing with seawater, barite precipitation
42 preferentially removes isotopically light Ba from vent fluids with a fractionation factor
43 of $\Delta^{138/134}\text{Ba}_{\text{hyd-barite-fluid}} = -0.35 \pm 0.10$ ‰ (2SE, n=2). Based on knowledge of barite
44 saturation and isotope fractionation during precipitation, the effective hydrothermal Ba
45 component that mixes with seawater after barite precipitation has completed can be
46 calculated: $\delta^{138/134}\text{Ba}_{\text{hyd}} = +1.7 \pm 0.7$ ‰ (2SD). This value is isotopically heavier than
47 deep ocean waters and may explain the observed non-conservative of Ba isotopes in
48 deep waters. These new constraints on hydrothermal Ba compositions enable the
49 hydrothermal input of Ba to Atlantic deep waters to be assessed at $\approx 3 - 9$ % of the

50 observed Ba. Barium isotopes might be used as a tracer to reconstruct the history of
51 hydrothermal Ba inputs and seawater SO₄ concentrations in the past.

52

53 **1. Introduction**

54 Mid-ocean ridge (MOR) hydrothermal systems play an important role in
55 determining seawater chemistry (Von Damm, 1990; Elderfield and Schultz, 1996;
56 German and Von Damm, 2003; Tivey, 2007; German and Seyfried, 2014; Humphirs
57 and Klein, 2018; Coogan et al., 2019). Hydrothermal systems are a source of some
58 elements to seawater (e.g. Fe, Mn and Li) and a sink for others (e.g. Mg and SO₄).
59 Hydrothermal vent fluids are enriched in Ba (1 ~ 119 μmol/kg) by up to 1000 times
60 relative to seawater (0.03 ~ 0.2 μmol/kg) (e.g. Butterfield et al., 1994; Charlou et al.,
61 1996; Von Damm et al., 1985; Kumagai et al., 2008; Seyfried et al. 2011).

62 Many processes control the hydrothermal flux of Ba into the ocean. Water-rock
63 interaction releases Ba from source rocks to vent fluids at elevated pressures and
64 temperatures (Von Damm et al., 1985). These source rocks contain Ba at the level of
65 [Ba] = 3.9 – 160.3 ppm in oceanic basalts (Gale et al., 2013) and [Ba] = 350 – 6230
66 ppm in marine sediments (Li and Schoonmaker, 2003), explaining the high Ba
67 concentration values in vent fluids. Mixing between these vent fluids and SO₄-bearing
68 seawater, however, leads to barite (BaSO₄) precipitation (e.g. Shikazono, 1994; Hanor,
69 2000; Seyfried et al. 2003; Jamieson et al., 2016; Gartman et al., 2019), which removes
70 Ba and reduces hydrothermal Ba input to seawater. Therefore, despite the fact that Ba
71 concentrations in vent fluids are several orders of magnitude higher than in seawater,
72 the ‘effective’ hydrothermal Ba input to the ocean is smaller and remains uncertain.

73 Barium isotopes have recently been studied as a new tracer to understand the
74 oceanic Ba cycle (Horner et al., 2015; Hsieh and Henderson, 2017; Bates et al., 2017;

75 Bridgestock et al., 2018; Crockford et al., 2019; Cao et al., 2020). In general, seawater
76 $\delta^{138/134}\text{Ba}$ values range from +0.22 to +0.65 ‰ in the global oceans. The deep Pacific
77 Ocean has higher Ba concentrations ($> 0.1 \mu\text{mol/kg}$) and lighter $\delta^{138/134}\text{Ba}$ values ($<$
78 $+0.3\text{‰}$) than the Atlantic Ocean. The main process controlling observed variations in
79 seawater $\delta^{138/134}\text{Ba}$ is barite formation and dissolution. This barite precipitation
80 preferentially removes light Ba isotopes from solutions into solid phases (e.g. von
81 Allmen et al., 2010; Böttcher et al., 2018).

82 The Ba isotope composition $\delta^{138/134}\text{Ba}$ of major inputs and outputs of Ba to the
83 ocean has been assessed. The main input to the ocean is from rivers and is isotopically
84 light, ranging from -0.06 to +0.46 ‰ (Cao et al., 2020; Hsieh and Henderson, 2017;
85 Gou et al., 2020). Estuaries also play an important role in the riverine Ba isotope
86 compositions through adsorption and desorption of Ba between suspended particles and
87 the dissolved phase (Gou et al., 2020). The main output is into marine sediments,
88 particularly as precipitated barite, and is also isotopically lighter than seawater, ranging
89 from -0.21 to +0.11 ‰ in suspended particles and pelagic sediments (Horner et al.,
90 2017; Bridgestock et al., 2018; Crockford et al., 2019). As yet, there are no available
91 data to constrain Ba isotope compositions in marine hydrothermal vent fluids.

92 The degree to which Ba isotopes behave conservatively in the deep ocean is
93 uncertain. Bates et al. (2017) suggested that Ba isotopes in deep ocean waters are mostly
94 conservative during the mixing between North Atlantic Deep Water (NADW, $\delta^{138/134}\text{Ba}$
95 $\approx +0.45\text{‰}$) and Antarctic Bottom Water (AABW, $\delta^{138/134}\text{Ba} \approx +0.25\text{‰}$), but Hsieh and
96 Henderson (2017) identified evidence for non-conservative mixing in deep waters, with
97 deviations towards higher $\delta^{138/134}\text{Ba}$ values than the conservative mixing trend,
98 particularly at depths of 2000 – 3000m (Fig. 1). Hydrothermal Ba inputs may be an
99 explanation for such non-conservative behavior.

100 In this study, we present the first Ba isotope data in hydrothermal vent fluids
101 from 6 hydrothermal systems in both the Atlantic and Pacific Oceans to establish the
102 relationship between vent fluid Ba isotope compositions and hydrothermal processes
103 (e.g. water-rock interaction and barite precipitation). We pair the dissolved and
104 particulate Ba data from the same hydrothermal vent fluids to understand the correlation
105 between barite precipitation and Ba isotope fractionation in hydrothermal systems.

106

107 **2. Materials and methods**

108 **2.1. Hydrothermal vent fluids and particles**

109 All the vent fluid and particle samples analyzed in this study were obtained by
110 the University of Minnesota co-authors over the past 15 years. The fluid samples (21
111 focused-flow and 10 diffuse-flow) were selected from 6 different hydrothermal systems
112 with distinct geologic settings along the mid-ocean ridges in both the Atlantic and
113 Pacific Oceans. Sites included are from the slow-spreading Mid-Atlantic Ridge (MAR):
114 Rainbow (36°N, ultramafic-hosted) and Trans Atlantic Geotraverse (TAG, 26°N, active
115 mound); the fast-spreading East Pacific Rise (EPR): 9-10°N and 13°N (basalt-hosted);
116 the intermediate-spreading Juan de Fuca Ridge (JdFR) in the Northeast Pacific: Main
117 Endeavor Field (MEF) (sediment-influenced) and ASHES vent field, Axial Caldera
118 (ASHES) (Fig. 2). Diffuse-flow samples generally refer to the MOR discharged vent
119 fluids at low temperature (relative to the high temperature focused-flow, > 250°C), low
120 flow rates and broad spatial distributions (Bemis et al., 2012). These fluids have
121 undergone variable mixing with seawater beneath the seafloor prior to venting. In this
122 study, only 3 of the 10 diffuse-flow samples have sufficient Ba for isotope analysis. To
123 assess the controls of Ba isotopes in diffuse-flow vent fluids, more data will be required.

124 Vent fluid samples were collected in a titanium syringe-type gas-tight sampling
125 device (Seewald et al., 2002; Wu et al., 2015). Initial ship-board processing of fluids
126 occurred within hours of sample recovery from the seafloor. In general, subsamples
127 were taken under pressure from each bottle for determination of pH (at 25°C), H₂S,
128 major dissolved anions and cations, and trace metals. The trace metal aliquot was
129 immediately acidified with high-purity HCl (Optima, Fisher Chemical) to pH ~1. A
130 fraction of this subsample (200 µL) was preserved in pre-weighed and acid-cleaned
131 polyethylene vials before sending to Oxford for analysis of Ba isotopes.

132 Precipitates that formed in the samplers upon cooling and mixing with entrained
133 seawater were rinsed with Milli-Q water, collected on a 0.2 µm nylon filter and
134 subsequently re-dissolved in HCl/HNO₃ (ULTREX, J.T. Baker). These precipitates are
135 commonly called “dregs”, and usually contain high levels of transition metals (e.g. Cu,
136 Fe, and Zn). Based on the metal contents, the mineralogy of dregs is mainly sulfides
137 (e.g. chalcopyrite and sphalerite) with other trace metals, such as As, Mo and Ba (Metz
138 and Trefry, 2000; Rouxel et al., 2008; Yucel et al., 2011; Gartman et al., 2014; Gartman
139 et al., 2018). Scanning electron microscopy (SEM) images show that Ba exists as barite,
140 surrounded by sulfides, in the particles precipitated in vent fluids (Gartman et al., 2018).
141 Precipitation of dregs reduces the concentrations or causes isotope fractionation in these
142 elements from the original fluids (Seyfried et al., 2003; Rouxel et al., 2008; James et
143 al., 2014). The amount of metals measured in the dregs was therefore recombined with
144 metals that remained in solution to obtain a complete metal inventory of the vent fluids
145 prior to collection. Dregs are not available for 10 vent fluid samples (out of 31) reported
146 here. These samples are mostly diffuse-flow type with no precipitation of dregs, except
147 for two focused-flow samples (4744-1 and 4744-2) where their dregs were not kept and

148 had no recorded Ba data. All fluid samples without dregs are reported as uncorrected
149 data only.

150 Sample ID (including sample years and submersible dive numbers), vent type,
151 location, and names are provided in Table 1, as are references to published data and
152 procedures that provide information critical to the broader interpretation of the Ba data
153 reported here. Vent fluid chemistries in these and other marine hydrothermal systems
154 have been well documented (e.g. Campbell et al., 1988; Butterfield et al., 1990; Von
155 Damm, 1990; Von Damm, 2000; Charlou et al., 2002; Douville et al., 2002; Seyfried
156 et al. 2003; Seyfried et al., 2011; Fornari et al., 2012). Most of the fluid samples
157 provided for this study have been analyzed and discussed for other trace elements and
158 isotopes in previous studies (Foustoukos and Seyfried, 2007; Foustoukos et al., 2009;
159 Pester et al., 2011; Seyfried et al., 2011; Pester et al., 2014; Syverson et al., 2017;
160 Scheuermann et al., 2018).

161

162 **2.2. Elemental concentrations analysis**

163 Most of the vent fluids and dregs samples reported here have been previously
164 analyzed for major and trace elements/species (Mg, Ca, Ba, Cl and SO₄) by ion
165 chromatography (IC) and inductively coupled plasma optical emission spectrometry
166 (ICP-OES) at the University of Minnesota. All the vent fluid Ba concentrations were
167 measured by isotope dilution (ID) thermal ionization mass spectrometer (TIMS) and
168 quadrupole (Quad) ICP-MS at the University of Oxford. The concentration unit of fluid
169 and dregs [Ba] was normalized to the weight of fluid ($[Ba]_{\text{fluid}} = \text{fluid Ba } \mu\text{mol}/\text{fluid kg}$;
170 $[Ba]_{\text{dregs}} = \text{dregs Ba } \mu\text{mol}/\text{fluid kg}$). For comparison, the data of [Ba] between ID-TIMS
171 and Quad-ICP-MS show agreement within 1-11% (Fig. S1). Therefore, we mainly use
172 the ID-TIMS [Ba] data in the discussion unless otherwise specified. Overall, the

173 precision of the elemental concentrations is around 1-3 % RSD. The total Ba
174 concentration was corrected ($[\text{Ba}]_{\text{corr}}$) by the sum of Ba concentrations in dissolved
175 fluids and dregs:

$$176 \quad [\text{Ba}]_{\text{corr}} = [\text{Ba}]_{\text{fluid}} + [\text{Ba}]_{\text{dregs}} \quad (1)$$

177

178 **2.3. Barium isotope analyses**

179 All the fluid solution samples were prepared and analyzed for Ba isotopes and
180 Ba concentrations using ID-TIMS at the University of Oxford. In addition to the fluid
181 samples, two of the dregs samples from MEF and ASHES were also analyzed for Ba
182 isotopes (Table 2). The Ba isotope methods were adapted from previous studies (Hsieh
183 and Henderson, 2017; Bridgestock et al., 2018). In brief, sample solutions, containing
184 ~200 ng of Ba or maximum 200 μL fluid, were weighed, acidified and spiked with
185 ^{137}Ba - ^{135}Ba double spike. The samples were dried and re-dissolved in 1mL 3M HCl
186 before purification by cation exchange chromatography (AG50-X8, 200-400 mesh).
187 The overall procedure blank is < 0.1 ng of Ba ($n = 3$). Barium isotope analyses were
188 performed on a Thermo Finnigan Triton TIMS at the University of Oxford. In this study,
189 Ba isotopic compositions are reported as the δ -notation $\delta^{138/134}\text{Ba}$ (‰) relative to the
190 National Institute of Standards and Technology (NIST) 3104a standard:

$$191 \quad \delta^{138/134}\text{Ba} (\text{‰}) = \left(\frac{^{138}\text{Ba}/^{134}\text{Ba}_{\text{sample}}}{^{138}\text{Ba}/^{134}\text{Ba}_{\text{NIST3104a}}} - 1 \right) \times 1000 \quad (2)$$

192 For comparison, data reported in $\delta^{137/134}\text{Ba}$ in some previous studies have been
193 converted to $\delta^{138/134}\text{Ba}$ by multiplying by 1.33.

194 Standards and samples generally show an internal precision between 0.01 and
195 0.02 ‰ ($\pm 2\text{SE}$, $n = 540$) during each isotope analysis. The long-term (external)
196 precision and accuracy are monitored with a secondary Ba standard NBS-127 over two
197 years, $\delta^{138/134}\text{Ba} = -0.29 \pm 0.02$ ‰ ($\pm 2\text{SD}$, $n = 14$), which is in agreement with published

198 values in previous studies (Horner et al., 2017; Crockford et al., 2019). We use the
199 repeatability of these standard measurements to assess uncertainty of single
200 measurement, which is generally quoted in this paper as $\pm 0.02\%$. Most measurements
201 had similar or better internal uncertainty (0.01-0.02 ‰, $\pm 2SE$) but a small number,
202 with low Ba contents, show larger internal uncertainty, up to 0.08 ‰ ($\pm 2 SE$). For these
203 samples, we use the internal uncertainty from their measurement.

204

205 **3. Results**

206 The hydrothermal vent fluids display a wide range of Ba concentrations from
207 0.43 to 97.9 $\mu\text{mol/kg}$ and $\delta^{138/134}\text{Ba}$ values from -0.26 to +0.91 ‰, including both dregs
208 corrected and uncorrected data, in selected hydrothermal fluids from six different vent
209 fields (Table 1; Fig. 3). For comparison, temperature, pH, Mg, Cl, Ca and SO_4 data are
210 provided in Table 1 and Table S1, and seawater data from the North Atlantic (Bates et
211 al., 2017; Hsieh and Henderson, 2017) and North Pacific (Geyman et al. 2019) are also
212 provided. No significant relationship was found between the $\delta^{138/134}\text{Ba}$ values and
213 temperature, pH, [Mg], [SO_4], [Ca] or [Cl] (all $r^2 < 0.1$). The fluid data show a
214 predictable linear relationship between SO_4 and Mg concentrations, which suggests a
215 conservative mixing between seawater and hydrothermal source fluid lacking these
216 components (Fig. 3a). In contrast, Ba concentrations broadly decrease with increasing
217 SO_4 concentrations due to seawater mixing (Fig. 3b). However, the relationship
218 between Ba and SO_4 concentrations is not linear, which indicates that Ba is removed
219 from solution during the mixing. The fluid $\delta^{138/134}\text{Ba}$ compositions broadly increase
220 with decreasing Ba concentrations, but this relationship cannot be explained by
221 conservative mixing between seawater and the endmember fluids either (Fig. 3c).

222 Different hydrothermal systems show a wide range of dissolved Ba isotope
223 compositions $\delta^{138/134}\text{Ba}$ and [Ba] (Table 1; Fig. 3c). Vent fluids from the ultramafic-
224 hosted Rainbow hydrothermal field (36°N, MAR) show $\delta^{138/134}\text{Ba}$ values from -0.26 to
225 +0.36 ‰, associated with a large gradient of [Ba] changing from 4.54 to 97.9 $\mu\text{mol/kg}$.
226 In the basalt-hosted EPR, the vent fluids from EPR 9-10°N and EPR 13°N show diverse
227 $\delta^{138/134}\text{Ba}$ values from +0.02 to +0.40 ‰ with a range of [Ba] from 0.43 to 14.1 $\mu\text{mol/kg}$.
228 In the JdFR, the $\delta^{138/134}\text{Ba}$ value is generally much heavier in the MEF and ASHES vent
229 fluids (+0.40 to +0.91 ‰) than is the case for the other vent fluids discussed, while the
230 Ba concentrations (1.65 to 46.1 $\mu\text{mol/kg}$) are not hugely different from the others.

231 Particulate (dregs) Ba concentrations show a wide range from below < 0.01
232 (below detection limit) to 41.2 $\mu\text{mol/kg}$. The sum of dregs Ba and dissolved fluid Ba
233 indicates the total content of Ba in the fluids, as calculated by Eq. (1) (Table 1). The
234 fraction of dregs Ba ranges from 2 to 83% of the total Ba. The dregs Ba isotopic
235 compositions $\delta^{138/134}\text{Ba}$ in two available samples are -0.11 ± 0.02 ‰ and $+0.08 \pm 0.08$
236 ‰, and both values are significantly lighter than their fluid $\delta^{138/134}\text{Ba}$ values (Table 2).
237 For comparison, the observed $\delta^{138/134}\text{Ba}$ compositions in hydrothermal barites also
238 show light values (-0.04 and -0.08 ‰, Crockford et al., 2019). The dregs isotope data
239 suggest that precipitation in the samplers has preferentially removed isotopically light
240 Ba from vent fluids, and that needs to be considered for the correction of $\delta^{138/134}\text{Ba}$
241 values in the vent fluids (see Discussion 4.2). The dregs corrected and uncorrected [Ba]
242 and $\delta^{138/134}\text{Ba}$ data are both reported in Table 1 for comparison, but the following
243 discussion is mainly based on the corrected data unless otherwise specified.

244

245 **4. Discussion**

246 **4.1. Barite saturation and precipitation during fluid-seawater mixing**

247 Vent fluid Ba and SO₄ concentrations show that Ba is removed during mixing
 248 with seawater (Fig. 3b). Such a correspondence has been observed in previous studies
 249 and has been explained by barite (BaSO₄) precipitation (Von Damm et al., 1985;
 250 Seyfried et al. 2003). Barite is one of the most common minerals formed during the
 251 mixing of Ba-bearing hydrothermal vent fluids and SO₄-bearing seawater (Shikazono,
 252 1994; Hanor, 2000; Jamieson et al., 2016; Gartman et al., 2019). Barite precipitation
 253 also often occurs during the sampling of high-temperature vent fluids as a result of
 254 seawater entrainment in the samplers, which has caused difficulty in determining the
 255 fluid endmember Ba concentrations (Butterfield and Massoth, 1994; Von Damm et al.,
 256 1985; Seyfried et al. 2003; Seyfried et al. 2011). Barite precipitation can also be induced
 257 by conductive cooling; reducing temperature decreases barite solubility and hence
 258 increases barite precipitation (Blount, 1977; Jamieson et al., 2016; Gartman et al., 2019).

259 Barite solubility experiments and thermodynamic models have been used to
 260 study Ba and SO₄ chemistry and assess barite saturation in different marine
 261 environments (Church and Wolgemuth, 1972; Blount, 1977; Monnin and Galinier,
 262 1988; Monnin, 1999; Monnin et al. 1999; Monnin et al. 2001). In this study, we apply
 263 the model of Monnin (1999) to calculate the barite solubility product (K_{sp}), activity
 264 coefficient (γ_{BaSO_4}) and barite saturation index (Ω_{barite}) in the fluid samples under the
 265 condition of mixing with deep seawater (1°C and 500 bar):

$$266 \quad \Omega_{barite} = IAP/K_{sp} \quad (3)$$

267 where IAP is the ionic activity product:

$$268 \quad IAP = [Ba^{2+}] \cdot [SO_4^{2-}] \cdot \gamma_{BaSO_4}^2 \quad (4)$$

269 where $[Ba^{2+}]$ and $[SO_4^{2-}]$ are the fluid Ba and SO₄ mole concentrations. The model
 270 parameters are $\text{Log}K_{sp} = -9.957$ and $\gamma_{BaSO_4} = 0.1442$ (Monnin, 1999).

271 The modeled curves of Ba and SO₄ concentrations at the equilibrium condition
272 $\Omega_{\text{barite}} = 1$ are plotted in Fig. 3b and the calculated Ω_{barite} values are reported in Table
273 S1. Most of the samples after the dregs correction are above the curve and the Ω_{barite}
274 values are greater than or close to 1, which implies that the fluid samples are mostly
275 supersaturated with respect to barite, except for one sample in EPR 9-10°N ($\Omega_{\text{barite}} =$
276 0.9). Given that the Ba concentration of this sample is higher than in seawater, where
277 the observed Ω_{barite} value is undersaturated, this suggests low degrees of seawater (and
278 therefore sulfate) entrainment during sampling. As the process of venting evolves,
279 barite precipitation can still occur with increased seawater mixing. The calculated
280 saturation index Ω_{barite} is likely to be overestimated in this study due to the
281 underestimate of solubility, particularly for the high temperature vent fluids.
282 Thermodynamic models show that barite K_{sp} decreases with increasing temperature,
283 but due to ion interactions and speciation changes, the solubility increases with
284 increasing temperature in NaCl bearing fluids (Blount, 1977; Monnin 1999).
285 Nevertheless, the chosen condition (1°C and 500 bar) is likely to represent the end point
286 of barite precipitation in hydrothermal plumes mixing with seawater, which provides
287 constraints on the barite precipitation during the entire process and hence the effective
288 input of hydrothermal Ba to the ocean.

289

290 **4.2. Precipitates in the fluids: correction and assessment of fractionation**

291 Precipitation of “dregs” from hydrothermal vent fluid often occurs in the
292 samplers during cooling and mixing with seawater. Although the mineralogy of dregs
293 is mainly metal sulfides (Metz and Trefry, 2000; Rouxel et al., 2008; Yucel et al., 2011;
294 Gartman et al., 2014; Gartman et al., 2018), Ba sulfide (BaS) is highly soluble in water,
295 which makes BaS unlikely to be the host for Ba in the dregs. One previous study has

296 shown that Ba exists as barite, surrounded by sulfides, in the particles precipitated in
297 vent fluids (Gartman et al., 2018). Ba is also commonly observed as barite in sulfide-
298 rich deposits and chimneys in hydrothermal systems (Koski et al., 1994; Shikazono,
299 1994; Tivey, 2007; James et al., 2014; Jamieson et al., 2016). Although these do not
300 exclude the possibility of having some Ba scavenged onto other mineral surfaces (e.g.
301 MnS) when samples are undersaturated for barite, barite seems to be the most likely
302 mineral to host the majority of Ba in the dregs when samples are supersaturated.

303 Correction for dregs is required to assess the original composition of the fluid
304 prior to precipitation. The calculation also enables an assessment of the isotope
305 fractionation occurring during precipitation. Initial fluid Ba isotope compositions were
306 corrected for precipitation of dregs using the analyses of the two dregs samples (Table
307 2; calculation details in supplementary material S1).

308 The average value of calculated $\Delta^{138/134}\text{Ba}_{\text{dregs-fluid}}$ is $-0.35 \pm 0.10 \text{ ‰}$ (2SE, n=2).
309 This agrees with values from barite precipitation in previous experimental studies
310 ($\Delta^{138/134}\text{Ba}_{\text{barite-fluid}} = -0.34 \pm 0.09 \text{ ‰}$, von Allmen et al., 2010), consistent with barite
311 being the major phase hosting Ba in the dregs. The results from previous experiments,
312 conducted between 4 and 80°C, have shown that Ba isotope fractionation has no
313 temperature dependence in barite precipitation (Von Allmen et al, 2010; Böttcher et al.,
314 2018). The similarity of observed fractionation at the higher temperatures of dregs
315 precipitation implies that this temperature independence may hold to the in situ
316 temperature of vent fluids (~350°C). Considering the uncertainties, the hydrothermal
317 barite Ba isotope fractionation factor is quite similar to that in pelagic barite
318 ($\Delta^{138/134}\text{Ba}_{\text{pelagic-barite-seawater}}$ ranging from -0.40 to -0.58 ‰, Hsieh and Henderson, 2017;
319 Horner et al., 2017; Bridgestock et al., 2018). Although the fractionation factor in
320 pelagic barite may be slightly larger, it possibly reflects the different precipitation

321 conditions and environment (e.g. microenvironment and bacteria for pelagic barite,
322 Bishop, 1998; Martinez-Ruiz et al., 2018).

323 The corrected $\delta^{138/134}\text{Ba}$ values in the fluids were made by using the measured
324 $\delta^{138/134}\text{Ba}_{\text{fluid}}$, $[\text{Ba}]_{\text{fluid}}$ and $[\text{Ba}]_{\text{dregs}}$ from each sample (Table 1; equation S3), assuming
325 that barite is the major phase hosting Ba in dregs and that it has a constant fractionation
326 factor ($\Delta^{138/134}\text{Ba}_{\text{hyd-barite-fluid}} = -0.35 \pm 0.10 \text{ ‰}$). Ba isotope compositions in four fluid
327 samples are not corrected for dregs due to the lack of dregs [Ba] data. The fractionation
328 factor can also be used in the Ba isotope fractionation model to explain the distribution
329 of hydrothermal vent fluid $\delta^{138/134}\text{Ba}$ values controlled by barite precipitation during
330 mixing with seawater (Discussion 4.4).

331

332 **4.3. Barium isotopes in endmember vent fluids**

333 Elemental compositions of endmember vent fluids are usually estimated by the
334 intersection of a regression line between elements and Mg or SO_4 concentrations at zero.
335 This approach relies on the assumption that endmember vent fluid Mg or SO_4 is zero,
336 and that any increase of Mg or SO_4 is due to seawater entrainment during sampling or
337 subsurface mixing (e.g. Von Damm et al., 1985). However, it is difficult to use the same
338 approach to determine the Ba compositions of endmember vent fluids due to barite
339 precipitation during mixing with seawater. Even after the dregs correction, the
340 corrected fluid Ba still shows non-conservative behavior (Fig. 3b), which implies that
341 either some barite precipitation has occurred in subsurface prior to venting of the fluids
342 or that there is a low recovery of dregs in the samplers. Thus, we select the vent fluids
343 with the highest Ba concentration (dregs corrected) from each hydrothermal vent field
344 as the estimates of endmember vent fluids, except for EPR9-10°N which takes the

345 average values of the three highest [Ba] samples. The endmember vent fluid [Ba] and
346 $\delta^{138/134}\text{Ba}$ values are summarized in Table 3 and Fig. 4.

347 Some difference in the endmember fluid Ba compositions can be found between
348 ultramafic-hosted (Rainbow, MAR 36°N), basalt-hosted (EPR) and sediment-
349 influenced (MEF) systems. The ultramafic-hosted endmember fluid (Rainbow) has the
350 highest [Ba] and lowest $\delta^{138/134}\text{Ba}$ values, although peridotite and serpentine, the most
351 common source rocks in the ultramafic-hosted systems, have a much lower Ba
352 concentration ([Ba]: 0.1-1.4 ppm, Andreani et al. 2014) than oceanic basalts ([Ba]: 3.9-
353 160.3 ppm, Gale et al. 2013). However, in a gabbro-bearing ultramafic system, such as
354 Rainbow, the components of plutonic and gabbroic rocks in the subsurface play an
355 important role in buffering the high temperature vent fluid chemistry (Seyfried et al.,
356 2011). These rocks may contain more Ba than the reported values above, but this
357 requires more knowledge of Ba in the ultramafic protolith. No reported $\delta^{138/134}\text{Ba}$ data
358 are available in peridotite and serpentine for direct comparison. The $\delta^{138/134}\text{Ba}$ value of
359 the basalt-hosted endmember fluids (EPR) is within the range of mid-ocean ridge basalt
360 (MORB) $\delta^{138/134}\text{Ba}$ values (+0.02 to +0.15‰) (Nielsen et al., 2018). The MEF vent fluid
361 chemistry has shown the encounter with sediments during the fluid recharge zones,
362 although MEF is not a sedimented MOR system (Lilley et al., 1993; Seyfried et al.,
363 2003). The high $\delta^{138/134}\text{Ba}$ value seen in the MEF endmember fluid may reflect the
364 influence of sediments.

365 Overall, the endmember fluid $\delta^{138/134}\text{Ba}$ values, ranging from -0.17 (\pm 0.07) to
366 +0.09 (\pm 0.03) ‰, are within the range of $\delta^{138/134}\text{Ba}$ values in their source rocks
367 (MORBs and altered oceanic crust (AOC): -0.09 to +0.33‰, Nielsen et al., 2018;
368 pelagic sediments: -0.2 to +0.1 ‰, Crockford et al., 2019 and Bridgestock et al., 2018)
369 (Fig. 4b). As expected, water-rock interaction at elevated temperatures and pressures

370 appears to occur without Ba isotope fractionation, and a similar observation has been
371 discovered for Ca isotopes (Scheuermann et al., 2018). Therefore, source rocks may be
372 used to constrain the endmember vent fluid $\delta^{138/134}\text{Ba}$ values.

373 Although the estimates of endmember vent-fluid Ba concentrations can be
374 affected by the uncertainty of Ba recovery in vent fluids, Ba isotopes may also provide
375 an approach to calculate the hypothetical concentration of the corrected Ba ($[\text{Ba}]_{\text{corr}^*}$)
376 in vent fluids prior to barite precipitation and the recovery of Ba (calculation details in
377 supplementary material S2). The $\delta^{138/134}\text{Ba}$ -derived hypothetical $[\text{Ba}]_{\text{corr}^*}$ and $[\text{Mg}]$
378 values can then be used to extrapolate the endmember fluid $[\text{Ba}]$ through a linear
379 regression line at the intercept of zero Mg (Fig. 5). In general, the correlations between
380 the fluid $[\text{Ba}]$ and $[\text{Mg}]$ are improved when using the $[\text{Ba}]_{\text{corr}^*}$ values. The extrapolated
381 endmember fluid $[\text{Ba}]$ values also agree with the highest fluid $[\text{Ba}]_{\text{corr}}$ values observed
382 in each vent field (Table 3), except for MEF (Fig. 5d). In MEF, the $[\text{Ba}]_{\text{corr}^*}$ values
383 correlate with the Ca and Cl concentrations in vent fluids (Fig. S3). Vapor rich fluids
384 with dissolved Cl contents below seawater are expected to have low endmember Ba
385 and Ca, because these species tend to partition into the liquid phase in the region of
386 liquid-vapor phase separation (Pester et al., 2015).

387 For future studies, Ba isotopes provide better constraints on the Ba
388 compositions in vent fluids if the endmember fluid $\delta^{138/134}\text{Ba}$ compositions can be
389 provided. The endmember fluid $\delta^{138/134}\text{Ba}$ values can be obtained by measuring fluid
390 samples with high Ba recovery and the source rocks for comparison.

391

392 **4.4. Barium isotope fractionation model: effective hydrothermal Ba input**

393 Hydrothermal input of dissolved Ba to the ocean is decreased by removal of Ba
394 due to barite precipitation during mixing between vent fluids and seawater. The impact

395 of this precipitation on Ba isotopes can be simply modelled using the known
396 fractionation during barite formation (e.g. von Allmen et al. 2010). This model can be
397 used to explain the variation of vent fluid $\delta^{138/134}\text{Ba}$ values, and the expected isotope
398 composition of Ba after barite precipitation.

399 We apply a Rayleigh isotope fractionation model:

$$400 \quad \delta^{138/134}\text{Ba}_{\text{fluid}} = \Delta^{138/134}\text{Ba}_{\text{hyd-barite-fluid}} \cdot \ln(f) + \delta^{138/134}\text{Ba}_{\text{endmember}} \quad (5)$$

401 where $\delta^{138/134}\text{Ba}_{\text{endmember}}$ and $\Delta^{138/134}\text{Ba}_{\text{hyd-barite-fluid}}$ denote the isotope composition of the
402 endmember fluids and hydrothermal barite isotope fractionation factor ($\Delta^{138/134}\text{Ba}_{\text{hyd-}}$
403 $\text{barite-fluid} = -0.35 \pm 0.10 \text{ ‰}$), respectively; f is the fraction of dissolved Ba remaining in
404 the fluids ($f = [\text{Ba}]_{\text{fluid}}/[\text{Ba}]_{\text{endmember}}$). The endmember fluid [Ba] and $\delta^{138/134}\text{Ba}$ values
405 from Table 3 are taken as the initial composition in each hydrothermal vent field.

406 A Rayleigh fractionation model is appropriate in this situation, because the
407 precipitation of barite is rapid and the exchange between formed barite and dissolved
408 Ba is likely limited. A similar fractionation model has been demonstrated in other
409 isotopes (e.g. Ca and Zn) in hydrothermal systems (Amini et al., 2008; John et al., 2008;
410 Syverson et al. 2018).

411 Vent fluid Ba isotope data mostly fit within the trajectory of the isotope
412 fractionation model with a constant fractionation factor $\Delta^{138/134}\text{Ba}_{\text{hyd-barite-fluid}} = -0.35 \pm$
413 0.10 ‰ (Fig 5). This suggests that the Ba isotope variation in vent fluids is primarily
414 driven by barite precipitation and that the fractionation factor is relatively constant
415 between all the vent fields of this study. There are, however, a few samples that cannot
416 be explained by the fractionation model with the initial $\delta^{138/134}\text{Ba}_{\text{endmember}}$ compositions.
417 These samples are mostly diffuse-flow type or have undergone significant phase
418 separation (Fig. 6). Such samples are likely to have differing initial Ba compositions,

419 and to reflect multiple Ba sources (e.g. non-basaltic Ba) and more complex circulation
420 environments.

421 The model can be used to calculate the Ba isotope compositions of the effective
422 hydrothermal component at the point of mixing where barite precipitation stops (Ω_{barite}
423 < 1) and the remaining hydrothermal dissolved Ba starts to mix conservatively with Ba
424 in seawater. Barite saturation calculations, using a seawater SO_4 concentration of 28
425 mmol/kg, indicate that fluids become undersaturated when $[\text{Ba}] < 0.2 \mu\text{mol/kg}$. We
426 extend the Rayleigh model to this value to assess the Ba isotope compositions at the
427 end point of hydrothermal plumes during mixing with seawater (Fig. 6e-h). These end-
428 point $\delta^{138/134}\text{Ba}$ compositions, representing the composition of dissolved Ba added to
429 seawater, are high (+1.0 ~ +2.6 ‰), with an average of $+1.7 \pm 0.7 \text{ ‰}$ (2SD).

430 In addition to barite precipitation, scavenging on to Fe oxyhydroxides and Mn
431 oxides may also remove Ba and cause isotope fractionation in hydrothermal plumes.
432 However, the fraction of Ba associated with the hydrothermal Fe oxyhydroxides is
433 relatively small in hydrothermal plumes (Feely et al. 1996). Barium scavenging onto
434 Fe oxyhydroxides or Mn oxides is likely to be a significantly less prominent process in
435 hydrothermal plumes, than incorporation into barite. Any isotope fractionation
436 associated with this process is unknown and would require future study to provide
437 further constraint.

438 Calculated end-point dissolved Ba compositions ($\delta^{138/134}\text{Ba} = +1.7 \pm 0.7 \text{ ‰}$) are
439 notably higher than the range observed in seawater (+0.22 ~ +0.65‰) (Fig. 4b). Such
440 an isotopically heavy Ba could explain the non-conservative mixing seen in Atlantic
441 deep waters (Hsieh and Henderson, 2017).

442

443 **4.5. Hydrothermal Ba isotopes and non-conservative mixing in deep waters**

444 To assess the influence of hydrothermal Ba input on the isotope composition of
 445 Atlantic deep-waters, a three endmember mixing model is applied to these waters:

$$446 \quad f_{\text{NADW}} + f_{\text{AABW}} + f_{\text{hyd}} = 1 \quad (6)$$

$$447 \quad [\text{Ba}]_{\text{sw}} = f_{\text{NADW}} [\text{Ba}]_{\text{NADW}} + f_{\text{AABW}} [\text{Ba}]_{\text{AABW}} + f_{\text{hyd}} [\text{Ba}]_{\text{hyd}} \quad (7)$$

$$448 \quad [\text{Ba}]_{\text{sw}} \cdot \delta^{138/134}\text{Ba}_{\text{sw}} = f_{\text{NADW}} \cdot [\text{Ba}]_{\text{NADW}} \cdot \delta^{138/134}\text{Ba}_{\text{NADW}} + f_{\text{AABW}} \cdot [\text{Ba}]_{\text{AABW}} \cdot \delta^{138/134}\text{Ba}_{\text{AABW}} \\ 449 \quad + f_{\text{hyd}} \cdot [\text{Ba}]_{\text{hyd}} \cdot \delta^{138/134}\text{Ba}_{\text{hyd}} \quad (8)$$

$$450 \quad F_{\text{Ba}_{\text{hyd}}} = f_{\text{hyd}} \cdot [\text{Ba}]_{\text{hyd}} / [\text{Ba}]_{\text{sw}} \quad (9)$$

451 where the subscripts identify the mixed deep seawater (sw) and each endmember:
 452 NADW, AABW and the effective hydrothermal Ba (hyd); f denotes the relative
 453 fractions of each endmember water, and $F_{\text{Ba}_{\text{hyd}}}$ is the relative fraction of hydrothermal
 454 Ba input in the Atlantic deep-waters.

455 The proximity of observed seawater compositions to these three end members
 456 constrains the mixture of these components, as illustrated in Fig. 7. The calculated
 457 fraction of hydrothermal plume water (f_{hyd}), the effective hydrothermal Ba endmember,
 458 is 1.3 ~ 3.6 % in the deep water, taking into account the uncertainty of endmember
 459 values. This assumes a combined two-stage water dilution factor of 1.4 ~ 3.6 ($\times 10^4$),
 460 firstly from vent fluids to the effective Ba endmember in the hydrothermal plume and
 461 then to the deep water, assuming a maximum dilution in the first stage of ≈ 500 (i.e.
 462 vent fluid [Ba] 100 $\mu\text{mol/kg}$ / 0.2 $\mu\text{mol/kg}$). The dilution factor is of a similar order of
 463 magnitude to the helium-3 dilution, 1.7 ~ 34 ($\times 10^4$): from vent fluids (endmember
 464 average ^3He : 17.1 pmol/kg, Jean-Baptiste et al., 2004) to deep waters ($^3\text{He} < 0.05$ to 1
 465 fmol/kg, Ruth et al., 2000 and Lupton, 1998). The calculated fraction of hydrothermal
 466 Ba input ($F_{\text{Ba}_{\text{hyd}}}$) consists of 3 ~ 9 % of the Ba in some Atlantic deep-waters. The
 467 deviations of seawater Ba isotopes from the conservative deep-water mixing can be

468 explained by different degrees of hydrothermal Ba contributions in deep waters (Fig.
469 7b).

470 The hydrothermal input contributes isotopically heavy Ba to the ocean
471 ($\delta^{138/134}\text{Ba} = +1.7 \pm 0.7 \text{ ‰}$) which, if a significant component of the ocean Ba cycle,
472 would be hard to reconcile with a balanced Ba isotope budget. Riverine Ba is the main
473 Ba input to the ocean with a range of measured isotope values from -0.06 to +0.46‰).
474 The major Ba output is biogenetic barite and its burial in marine sediments which has
475 a $\delta^{138/134}\text{Ba}$ value from -0.21 to +0.11‰. This range overlaps that of rivers (Fig. 4b) but
476 may be somewhat lower on average, so that observed inputs may be isotopically heavier
477 than outputs. The heavy input from hydrothermal Ba implies that either (1)
478 hydrothermal Ba flux is small; or (2) other isotopically heavy sinks are missing. The
479 total global hydrothermal Ba vent flux has been estimated to be 2.40 to 3.35 Gmol/yr
480 (Paytan and Kastner, 1996; Dickens et al., 2003), based on the end-member vent fluid
481 [Ba] prior to barite precipitation (i.e. with Ba concentration $> 10 \mu\text{mol/kg}$, Von Damm
482 et al., 1985). This flux is about 4 ~ 6 times smaller than the riverine Ba flux (14.75
483 Gmol/yr, Wolgemuth and Broecker, 1970; Dickens et al., 2003). Considering that
484 hydrothermal [Ba], after precipitation of barite, is $0.2 \mu\text{mol/kg}$, the effective
485 hydrothermal Ba flux to the global ocean will be much smaller than the initial vent flux.
486 More precise assessments of Ba fluxes and isotopic compositions in other sources (e.g.
487 cold seeps and submarine groundwater discharge) and sinks (e.g. Fe-Mn oxides and
488 oxyhydroxides) are needed to fully constrain the Ba isotope budget in the ocean.

489 Seawater SO_4 plays an important role in barite saturation and hence in
490 determining the influence of hydrothermal Ba input and its non-conservative behavior
491 in the ocean. In an ocean with lower SO_4 concentration than the modern ocean, barite
492 precipitation during mixing would cease at a higher Ba concentration, and consequently

493 lower $\delta^{138/134}\text{Ba}$ value (Fig. 8). Reconstructions of marine sulfur isotope values suggest
494 that seawater SO_4 concentration may have varied from present levels to much lower
495 concentrations of only a few mmol/kg during the Phanerozoic (Canfield and Farquhar,
496 2009; Turchyn and DePaolo, 2019). These changes could have a large impact on the
497 hydrothermal Ba inputs to the ocean. Deep sea corals (Hemsing et al., 2017; Geyman
498 et al., 2019) and hydrothermal barites (Crockford et al., 2019) can potentially be used
499 to reconstruct water and hydrothermal Ba isotope compositions in the past. The
500 relationship between seawater SO_4 and barite precipitation may allow Ba and Ba
501 isotopes to serve as a tracer to reveal the history of MOR hydrothermal Ba inputs and
502 seawater SO_4 in the ocean.

503

504 **5. Conclusions**

505 We present the first Ba isotope data in MOR hydrothermal vent fluids from
506 numerous hydrothermal systems, including basalt-hosted, ultramafic-hosted and
507 sediment-influenced hydrothermal systems. The vent fluids display a wide range of
508 dissolved Ba concentrations and are generally supersaturated with respect to barite
509 ($\Omega_{\text{barite}} > 1$). The endmember initial vent fluid $\delta^{138/134}\text{Ba}$ values, ranging from -0.17 to
510 +0.09 ‰, agree with the values observed in source rocks, which implies that water-rock
511 interaction has a limited effect on the Ba isotope variation in vent fluids. Barite
512 precipitation removes isotopically light Ba from vent fluids during the mixing between
513 Ba-bearing vent fluids and SO_4 -bearing seawater. This mixing follows a Rayleigh
514 fractionation with a fractionation factor of $\Delta^{138/134}\text{Ba}_{\text{hyd-barite-fluid}} = -0.35 \pm 0.10$ ‰. Barite
515 precipitation controls the magnitude and composition of hydrothermal Ba input
516 ultimately added as dissolved Ba to seawater. The effective hydrothermal Ba
517 composition is calculated as $[\text{Ba}]_{\text{hyd}} = 0.2$ $\mu\text{mol/kg}$ and $\delta^{138/134}\text{Ba}_{\text{hyd}} = +1.7 \pm 0.7$ ‰.

518 Such an isotopically heavy Ba can explain the non-conservative mixing seen in deep
519 waters, with hydrothermal input around 3 ~ 9 % of the Ba in some Atlantic deep waters.
520 The relationship between vent fluid Ba and seawater SO₄ makes Ba isotopes a potential
521 tracer to reconstruct the history of MOR hydrothermal Ba inputs and seawater SO₄
522 concentrations in the past.

523

524 **Acknowledgements**

525 We thank Phil Holdship for his assistance with the Quad-ICP-MS analysis. We would
526 also like to thank John Higgins for discussion. Moreover, we wish to thank the captain
527 and crew of UNOLS ships and support vehicles (U.S.) for their assistance in planning
528 and execution, without which the vent fluid samples reported here would not have been
529 possible. Vent fluid sampling studies conducted by University of Minnesota researchers
530 benefited as well from efforts of students and staff scientists. These field and related
531 experimental studies were supported through US NSF grants: 0549547, 0751771,
532 0813861, 0961188 and 1736679 (WES). The Associate Editor and three anonymous
533 reviewers are appreciated for their valuable comments to improve this paper.

534 **References**

535

536 Amini M., Eisenhauer, A., Böhm, F., Fietzke, J., Bach, W., Garbe-Schönberg, D.,
537 Rosner, M., Bock, B., Lackschewitz, K. S. and Hauff, F. (2008) Calcium isotope
538 ($\delta^{44/40}\text{Ca}$) fractionation along hydrothermal pathways, Logatchev field (Mid-Atlantic
539 Ridge, 14°45'N). *Geochimica et Cosmochimica Acta* **72**, 4107–4122.

540

541 Andreani, M., Escartin, J., Delacour, A., Ildefonse, B., Godard, M., Dymont, J., Fallick,
542 A. E. and Fouquet Y. (2014) Tectonic structure, lithology, and hydrothermal signature
543 of the Rainbow massif (Mid-Atlantic Ridge 36°14'N). *Geochemistry, Geophysics,*
544 *Geosystems* **15**, 3543–3571.

545

546 Bates S. L., Hendry, K. R., Pryer, H. V., Kinsley, C. K., Pyle, K. M., Woodward, E. M.
547 and Horner, T. J. (2017) Barium isotopes reveal role of ocean circulation on barium
548 cycling in the Atlantic. *Geochimica et Cosmochimica Acta* **204**, 286-299.

549

550 Bemis, K., Lowell, R. P. and Farough., A. (2012) Diffuse flow on and around
551 hydrothermal vents at mid-ocean ridges. *Oceanography* **25**, 182–191.

552
553 Bishop, J. K. B. (1998) The barite-opal-organic carbon association in oceanic
554 particulate matter. *Nature* **332**, 341-343.
555
556 Blount, C. W. (1977) Barite solubilities and thermodynamic quantities up to 300°C and
557 1400 bars. *American Mineralogist* **62**, 942-957.
558
559 Böttcher M. E, Neubert, N., von Allmen, K., Samankassou, E. and Nagler, T. F. (2018)
560 Barium isotope fractionation during the experimental transformation of aragonite to
561 whiterite and of gypsum to barite, and the effect of ion (de)solvation. *Isotopes in*
562 *Environmental and Health Studies* **54**, 324-335.
563
564 Bridgestock, L., Hsieh, Y-T., Porcelli, D., Homoky, W. B., Bryan, A. and Henderson,
565 G. M. (2018) Controls on the barium isotope compositions of marine sediments. *Earth*
566 *and Planetary Science Letters* **481**, 101-110.
567
568 Butterfield, D. A., Massoth, G. J., McDuff, R. E., Lupton, J. E. and Lilley, M. D. (1990)
569 Geochemistry of hydrothermal fluids from Axial Seamount hydrothermal emissions
570 study vent field, Juan de Fuca Ridge: Subseafloor boiling and subsequent fluid-rock
571 interaction. *Journal of Geophysical Research* **95**, 12895-12921.
572
573 Butterfield, D. A., McDuff, R. E., Mottl, M. J., Lilley, M. D., Lupton, J. E.
574 and Massoth, G. J. (1994) Gradients in the composition of hydrothermal fluids from the
575 Endeavor segment vent field: Phase separation and brine loss, *Journal of Geophysical*
576 *Research* **99**, 9561–9583.
577
578 Butterfield, D. A. and Massoth, G. J. (1994) Geochemistry of north Cleft segment vent
579 fluids: temporal changes in chlorinity and their possible relation to recent
580 volcanism. *Journal of Geophysical Research* **99**, 4951-4968.
581
582 Campbell, A. C., Palmer, M. R., Klinkhammer, G. P., Bowers, T. S., Edmond, J. M.,
583 Lawrence, J. R., Casey, J. F., Thompson, G., Humphris, S., Rona, P. and Karson, J. A.
584 (1988) The chemistry of hot springs on the Mid-Atlantic Ridge. *Nature* **335**, 514–519.
585
586 Canfield, D. E., and Farquhar, J. (2009) Animal evolution, bioturbation, and the sulfate
587 concentration of the oceans. *Proceedings of the National Academy of Sciences of the*
588 *United States of America* **106**, 8123-8127.
589
590 Cao, Z., Siebert, C., Hathorne, E. C., Dai, M. and Frank, M. (2020) Corrigendum to
591 “Constraining the oceanic barium cycle with table barium isotopes” [Earth Planet. Sci.
592 Lett. 434 (2016) 1-9]. *Earth and Planetary Science Letters* **530**, 116003.
593
594 Cao, Z., Sibert, C., Hathorne, E. C., Dai, M. and Frank, M. (2016) Constraining the
595 oceanic barium cycle with table barium isotopes. *Earth and Planetary Science Letters*
596 **434**, 1-9.
597
598 Charlou, J. L., Fouquet, Y., Donval, J. P., Auzende, J. M., Jean-Baptiste, P., Stievenard,
599 M. and Michel, S. (1996) Mineral and gas geochemistry of hydrothermal fluids on an
600 ultrafast spreading ridge: East Pacific Rise, 17° to 19°S (Naudur cruise, 1993) - phase

601 separation processes controlled by volcanic and tectonic activity. *Journal of*
602 *Geophysical Research* **101**, 15899-15919.

603

604 Charlou, J. L., Donval, J. P., Fouquet, Y., Jean-Baptiste, P. and Holm, N. (2002)
605 Geochemistry of high H₂ and CH₄ vent fluids issuing from ultramafic rocks at the
606 Rainbow hydrothermal field (36°14'N, MAR). *Chemical Geology* **191**, 345–359.

607

608 Church, T. M. and Wolgemuth, K. (1972) Marine barite saturation. *Earth and Planetary*
609 *Science Letters* **15**, 35-44.

610

611 Coogan, L. A., Seyfried, W. E., Jr., and Pester, N. J. (2019) Environmental controls on
612 mid-ocean ridge hydrothermal fluxes. *Chemical Geology* **528**, 119285.

613

614 Crockford, P. W., Wing, B. A., Paytan, A., Hodgskiss, M. S. W., Mayfield, K. K.,
615 Hayles, J. A., Middleton, J. E., Ahn, A-S. C., Johnson, D. T., Caxito, F., Uhlein, G.,
616 Halverson, G. P., Eickmann, B., Torres, M. and Horner, T. J. (2019) Barium-isotopic
617 constraints on the origin of post-Marinoan barites. *Earth and Planetary Science* **519**,
618 234-244.

619

620 Dickens, G. R., Fewless, T., Thomas, E. and Bralower T. J. (2003) Excess barite
621 accumulation during the Paleocene-Eocene Thermal Maximum: Massive input of
622 dissolved barium from seafloor gas hydrate reservoirs, *in* Ginerich, P. et al., eds.,
623 Causes and consequences of globally warm climates in the early Paleogene: Geological
624 Society of America Special Paper **369**, 11-23.

625

626 Douville, E., Charlou, J. L., Oelkers, E. H., Biennu, P., Jove Colon, C. F., Donval, J.
627 P., Fouquet, Y., Prieur, D. and Appriou, P. (2002) The Rainbow vent fluids
628 (36°14'N, MAR): the influence of ultramafic rocks and phase separation on trace metal
629 content in Mid-Atlantic Ridge hydrothermal fluids. *Chemical Geology* **184**, 37–48.

630

631 Elderfield, H. and Schultz, A. (1996) Mid-ocean ridge hydrothermal fluxes and the
632 chemical composition of the ocean. *Annual Reviews of Earth and Planetary Sciences*
633 **24**, 191-224.

634

635 Feely, R. A., Baker, E. T., Marumo, K., Urabe, T., Ishibashi, J., Gendron, J., Lebon, G.
636 T., Okamura, K. (1996) Hydrothermal plume particles and dissolved phosphate over
637 the superfast-spreading southern East Pacific Rise. *Geochimica et Cosmochimica Acta*
638 **60**, 2297-2323.

639

640 Fornari, D. J., Von Damm, K. L., Bryce, J. G., Cowen, J. P., Ferrini, V., Fundis, A.,
641 Lilley, M. D., Luther III, G. W., Mullineaux, L. S., Perfit, M. R., Meana-Prado, M. F.,
642 Rubin, K. H., Seyfried Jr., W. E., Shank, T. M., Soule, S. A., Tolstoy, M. and White, S.
643 M. (2012) The East Pacific Rise between 9°N and 10°N: Twenty-five years of
644 integrated, multidisciplinary oceanic spreading center studies. *Oceanography* **25**, 18–
645 43.

646

647 Foustoukos, D. I. and Seyfried, W.E., Jr. (2007) Quartz solubility in the two-phase and
648 critical region of the NaCl-KCl-H₂O system: Implications for submarine hydrothermal
649 vent systems at 9°50'N East Pacific Rise. *Geochimica et Cosmochimica Acta* **71**, 186-
650 201.

651
652 Foustoukos, D. I., Pester, N. J., Ding, K. and Seyfried, W. E. (2009) Dissolved carbon
653 species in associated diffuse and focused flow hydrothermal vents at the Main
654 Endeavour Field, Juan de Fuca Ridge: phase equilibria and kinetic constraints.
655 *Geochemistry, Geophysics, Geosystems* **10**, Q10003
656
657 Gale, A., Dalton, C. A., Langmuir, C. H., Su, Y. and Schilling J.-G (2013) The mean
658 composition of ocean ridge basalts. *Geochemistry, Geophysics, Geosystems* **14**, 489-
659 518.
660
661 Gartman, A., Findlay, A. J., Hannington, M., Garbe-Schonbert, D., Jamieson, J. W. and
662 Kwasnitschka T. (2019) The role of nanoparticles in mediating element deposition and
663 transport at hydrothermal vents. *Geochimica et Cosmochimica Acta* **261**, 113-131.
664
665 Gartman, A., Hannington, M., Jamieson, J. W., Peterkin, B., Garbe-Schonberg, D.,
666 Findlay, A. J., Fuchs, S. and Kwasnitschka, T. (2018) Boiling-induced formation of
667 colloidal gold in black smoker hydrothermal fluids. *Geology* **46**, 39-42.
668
669 Gartman, A., Findlay, A. J. and Luther, G. W. (2014) Nanoparticulate pyrite and other
670 nanoparticles are a widespread component of hydrothermal vent black smoker
671 emissions. *Chemical Geology* **366**, 32-41.
672
673 German, C. and Von Damm, K. (2003) Hydrothermal processes.
674 H. Elderfield (Ed.), *Treatise on Geochemistry: The Oceans and Marine*
675 *Geochemistry*, Elsevier/Pergamon, Oxford, pp. 181-222.
676
677 German, C. and Seyfried, W.E., Jr. (2014) Hydrothermal Processes. *The Oceans &*
678 *Marine Geochemistry. Treatise on Geochemistry Series*, vol. 8. Pp. 191-233.
679
680 Geyman, B. M., Ptacek, J. L., LaVigne, M., and Horner, T. J. (2019) Barium in deep-
681 sea bamboo corals: Phase associations, barium stable isotopes, & prospects for
682 paleoceanography. *Earth and Planetary Science Letters* **525**, 115751.
683
684 Gou, L., Jon, Z., Galy, A., Gong, Y., Nan, C. J., Wnag, X., Bouchez, J., Cai, H., Chen,
685 J., Yu, H. and Huang, F. (2020) Seasonal riverine barium isotopic variation in the
686 middle Yellow River: Sources and Fractionation. *Earth and Planetary Science Letters*
687 **531**, 115990.
688
689 Hanor, J. S. (2000) Barite-celestine geochemistry and environments of formation.
690 C.N. Alpers, J.L. Jambor, D.K. Nordstrom (Eds.), *Reviews in Mineralogy &*
691 *Geochemistry – Sulfate Minerals*, Vol. 40, Mineralogical Society of
692 America, Washington, D.C., pp. 193-275
693
694 Hemsing, F., Hsieh Y-T., Bridgestock, L., Spooner, P. T., Robinson, L., F., Frank, N.
695 and Henderson, G. M. (2018) Barium isotopes in cold-water corals. *Earth and*
696 *Planetary Science Letters* **491**, 183-192.
697
698 Humphris, S.E. and Klein F. (2018) Progress in deciphering the controls on the
699 geochemistry of fluids in seafloor hydrothermal systems. *Annu. Rev. Mar. Sci.* **10**, 315-
700 343.

701
702
703 Horner, T. J., Kinsley, C. W. and Nielsen, S. G. (2015) Barium-isotopic fractionation
704 in seawater mediated by barite cycling and oceanic circulation. *Earth and Planetary*
705 *Science Letters* **430**, 511-522.
706
707 Horner, T. J., Pryer, H. V., Nielsen, S. G., Crockford, P. W., Gauglitz, J. M., Wing, B.
708 A. and Ricketts, R. D. (2017) Pelagic barite precipitation at micromolar ambient sulfate.
709 *Nature Communications* **8**, 1242.
710
711 Hsieh, Y-T. and Henderson, G. M. (2017) Barium stable isotopes in the global ocean:
712 Tracer of Ba inputs and utilization. *Earth and Planetary Science Letters* **473**, 269-278.
713
714 James, R. H., Green, D. R. H., Stock, M. J., Alker, B. J., Banerjee, N. R., Cole, C.,
715 German, C. R., Huvenne, V. A. I., Powell, A. M. and Connelly, D. P. (2014)
716 Composition of hydrothermal fluids and mineralogy of associated chimney material on
717 the East Scotia Ridge back-arc spreading centre. *Geochimica et Cosmochimica Acta*
718 **139**, 47-71.
719
720 Jamieson, W. D., Hannington M. D., Tivey, M. K., Hansteen, T., Williamson, N. M.
721 B., Steward, M., Fietzke, J., Butterfield, D., Frische, M., Allen, L., Cousens, B. and
722 Langer, J., (2016) Precipitation and growth of barite within hydrothermal vent deposits
723 from the Endeavour Segment, Juan de Fuca Ridge. *Geochimica et Cosmochimica Acta*
724 **173**, 64-85.
725
726 Jean-Baptiste, P., Fourre, E., Charlou, J. L., German, C. R. and Radford-Knoery, J.
727 (2004) Helium isotopes at the Rainbow hydrothermal site (Mid-Atlantic Ridge,
728 36°14'N). *Earth and Planetary Science Letters* **221**, 325-335.
729
730 John, S., Rouxel, O., Craddock, P., Engwall, A., Boyle E. (2008) Zinc stable isotopes
731 in seafloor hydrothermal vent fluids and chimneys. *Earth and Planetary Science Letters*
732 **269**, 17-28.
733
734 Koski, R. A., Jonasson, I. R., Kadko, D. C., Smith, V. K., and Wong, F. L. (1994)
735 Compositions, growth mechanisms, and temporal relations of hydrothermal sulfide-
736 sulfate-silica chimneys at the northern Cleft Segment, Juan de Fuca Ridge, *Journal of*
737 *Geophysical Research Solid Earth* **99**, 4813-4832.
738
739 Kumagai, H., Nakamura, K., Toki, T., Morishita, T., Okino, K., Ishibashi, J. I.,
740 Tsunogai, U., Kawagucci, S., Gamo, T., Shibuya, T., Sawaguchi, T., Neo, N.,
741 Joshima, M., Sato, T. and Takai, K. (2008) Geological background of the Kairei and
742 Edmond hydrothermal fields along the Central Indian Ridge: implications of their vent
743 fluids' distinct chemistry *Geofluids* **8**, 239-251.
744
745 Li, Y.-H. and Schoonmaker, J.E. (2003) Chemical composition and mineralogy of
746 marine sediments. *Treatise on Geochemistry* **7**, 1-35.
747
748 Lilley, M. D., Butterfield, D. A., Olson, E. J., Lupton, J. E., Macko, S. A. and McDuff,
749 R.E. (1993) Anomalous CH₄ and NH₄⁺ concentrations at an unsedimented mid-ocean-
750 ridge hydrothermal system. *Nature* **364**, 45-47.

751
752 Lupton, J. (1998) Hydrothermal helium plumes in the Pacific Ocean. *Journal of*
753 *Geophysical Research* **103**, 15853-15868.
754
755 Martinez-Ruiz, F., Jroundi, F., Paytan, A., Guerra-Tschuschke, I., Abad, M. M., and
756 Gonzalez-Munoz, M. T. (2018) Barium bioaccumulation by bacterial biofilms and
757 implications for Ba cycling and use of Ba proxies. *Nature Communications* **9**, 1619.
758
759 Metz, S. and Trefry, J. H. (2000) Chemical and mineralogical influences on
760 concentrations of trace metals in hydrothermal fluids. *Geochimica et Cosmochimica*
761 *Acta* **64**, 2267-2279.
762
763 Monnin, C. and Galinier C. (1988) The solubility of celestite and barite in electrolyte
764 solutions and natural waters at 25°C: A thermodynamic study. *Chemical Geology* **71**,
765 283-296.
766
767 Monnin, C. (1999) A thermodynamic model for the solubility of barite and celestite in
768 electrolyte solutions and seawater from 0 to 200°C and to 1 kbar. *Chemical Geology*
769 **153**, 187–209.
770
771 Monnin, C., Jeandel, C., Cattaldo, T. and Dehairs, F. (1999) The marine barite
772 saturation state of the world's oceans. *Marine Chemistry* **65**, 253-261.
773
774 Monnin, C., Wheat C. G, Dupre B., Elderfield H. and Mottl M. M. (2001) Barium
775 geochemistry in sediment porewaters and formation waters of the oceanic crust on
776 eastern flank of the Juan de Fuca ridge (ODP Leg 168). *Geochemistry, Geophysics,*
777 *Geosystems*, 2000GC000073.
778
779 Nielsen, S. G., Horner, T. J., Pryer, H. V., Blusztajn, J., Shu, Y., Kurz, M. D. and Le
780 Roux, V. (2018) Barium isotope evidence for pervasive sediment recycling in the upper
781 mantle. *Science Advances* **4**, eaas8675
782
783 Nielsen, S. G., Shu, Y., Auro, M., Yogodzinski, G., Shinjo, R., Plank, T., Kay, S. M.
784 and Horner, T. J. (2020) Barium isotope systematics of subduction zones. *Geochimica*
785 *et Cosmochimica Acta* **275**, 1-18.
786
787 Paytan, A and Kastner, M. (1996) Benthic Ba fluxes in the central Equatorial Pacific,
788 implications for the oceanic Ba cycle, *Earth and Planetary Science Letters* **142**, 439-
789 450
790
791 Pester, N. J., Rough, M., Ding, K., Seyfried, W. E., Jr. (2011) A new Fe/Mn
792 geothermometer for hydrothermal systems: implications for high-salinity fluids at 13
793 N on the East Pacific Rise. *Geochimica et Cosmochimica Acta* **75**, 7881-7892.
794
795 Pester, N. J., Ding, K. and Seyfried, W. E., Jr. (2014) Magmatic eruptions and iron
796 volatility in deep-sea hydrothermal fluids. *Geology* **42**, 255-258.
797
798 Pester, N. J., Ding, K. and Seyfried, W. E. Jr. (2015) Vapor–liquid partitioning of
799 alkaline earth and transition metals in NaCl-dominated hydrothermal fluids: An

800 experimental study from 360 to 465°C, near-critical to halite saturated conditions.
801 *Geochimica et Cosmochimica Acta* **168**, 111-132.

802
803 Ruth, C., Well, R. and Roether, W. (2000) Primordial ³He in South Atlantic deep
804 waters from sources on the Mid-Atlantic Ridge. *Deep Sea Research Part I* **47**, 1059-
805 1075.

806
807 Rouxel, O., Shanks, W. C., Bach, W. and Edwards, K. J. (2008) Integrated Fe- and S-
808 isotope study of seafloor hydrothermal vents at East Pacific rise 9-10°N. *Chemical*
809 *Geology* **252**, 214-227.

810
811 Scheuermann, P. P., Syverson, D. D., Higgins, J. A., Pester, N. J. and Seyfried, W. E.,
812 Jr. (2018) Calcium isotope systematic at hydrothermal conditions: Mid-ocean ridge
813 vent fluids and experiments in the CaCO₄-NaCl-H₂O system. *Geochimica et*
814 *Cosmochimica Acta* **226**, 18-35.

815
816 Seewald, J. S., Doherty, K. W., Hammar, T. R. and Liberatore, S. P. (2002) A new gas-
817 tight isobaric sampler for hydrothermal fluids. *Deep Sea Research Part I:*
818 *Oceanographic Research Papers* **49**, 189-196.

819
820 Seyfried, W. E., Jr., Seewald, J. S., Berndt, M. E., Ding, K. and Foustoukos D. I. (2003)
821 Chemistry of hydrothermal vent fluids from the Main Endeavour Field, northern Juan
822 de Fuca Ridge: Geochemical controls in the aftermath of June 1999 seismic events.
823 *Journal of Geophysical Research: Solid Earth* **108**, 1-23.

824
825 Seyfried, W. E., Jr., Pester, N. J., Ding, K. and Rough, M. (2011) Vent fluid chemistry
826 of the Rainbow hydrothermal system (36°N, MAR): Phase equilibria and in situ pH
827 controls on subseafloor alteration processes. *Geochimica et Cosmochimica Acta* **75**,
828 1574-1593.

829
830 Shikazono, N., (1994) Precipitation mechanisms of barite in sulfate-sulfide deposits in
831 back-arc basins. *Geochimica et Cosmochimica Acta* **58**, 2203-2213.

832
833 Syverson, D. D., Luhmann, A. J., Tan, C. Y., Borrok, D. M., Ding, K. and Seyfried, W.
834 E., Jr. (2017) Fe isotope fractionation between chalcopyrite and dissolved Fe during
835 hydrothermal recrystallization: An experimental study at 350 degrees C and 500 bars.
836 *Geochimica et Cosmochimica Acta* **200**, 87-109.

837
838 Syverson, D. D., Scheuermann, P., Higgins, J. A., Pester, N. J., Seyfried, W. E., Jr.
839 (2018) Experimental partitioning of Ca isotopes and Sr into anhydrite: Consequences
840 for the cycling of Ca and Sr in subseafloor mid-ocean ridge hydrothermal systems.
841 *Geochimica et Cosmochimica Acta* **236**, 160-178.

842
843 Tivey, M. K. (2007) Generation of seafloor hydrothermal vent fluids and associated
844 mineral deposits. *Oceanography* **20**, 50-65.

845
846 Turchyn, A. V. and DePaolo, D. J. (2019) Seawater chemistry through Phanerozoic
847 time. *Annual Reviews of Earth and Planetary Sciences* **47**, 197-224.

848

849 von Allmen, K., Bottcher, M. E., Samankassou, E. and Nagler, T. F. (2010) Barium
850 isotope fractionation in the global barium cycle: First evidence from barium minerals
851 and precipitation experiments. *Chemical Geology* **277**, 70-77.
852
853 Von Damm, K. L., Edmond, J. M., Grant, B., Measures, C. I., Walden, B. and Weiss,
854 R. F. (1985) Chemistry of submarine hydrothermal solutions at 21°N, East Pacific Rise.
855 *Geochimica et Cosmochimica Acta* **49**, 2191-2220.
856
857 Von Damm, K. L. (1990) Seafloor hydrothermal activity – Black smoker chemistry and
858 chimneys. *Annual Reviews of Earth and Planetary Sciences* **18**, 173-204.
859
860 Von Damm, K. L. (2000) Chemistry of hydrothermal vent fluids from 9°-10°N, East
861 Pacific Rise: “Time zero,” the immediate post-eruptive period. *Journal of Geophysical*
862 *Research* **105**, 11203-11222.
863
864 Wolgemuth, K., and Broecker, W. S. (1970) Barium in sea water, *Earth and*
865 *Planetary Science Letters* **8**, 372-378.
866
867 Wu, S.-J., Yang, C.-J., Ding, K. and Tan, C. (2015) A remotely operated serial sampler
868 for collecting gas-tight fluid samples. *China Ocean Engineering* **29**, 783-792.
869
870 Yucel, M., Gartman, A., Chan, C. S. and Luther, G. W. (2011) Hydrothermal vents as
871 a kinetically stable source of iron-sulphide-bearing nanoparticles to the ocean. *Nature*
872 *Geoscience* **4**, 367-371.
873

874 **Table and figure captions**

875 **Table 1** Vent fluid and particle (dregs) sample information, temperature, Mg, SO₄ and
876 Ba concentrations and Ba isotope compositions.

877 **Table 2** Vent fluid and particle (dregs) Ba concentration, isotope composition and
878 fractionation factor.

879 **Table 3** Summary of calculated Ba compositions in endmember fluids.

880

881 **Figure 1.** Compilations of seawater [Ba] and $\delta^{138/134}\text{Ba}$ data below 2000 m in the
882 Atlantic and Southern Oceans. Deep-water $\delta^{138/134}\text{Ba}$ and [Ba] data in the South
883 Atlantic (2000~3000 m) show deviations ($\sim 0.1\%$ $\delta^{138/134}\text{Ba}$ offsets), highlighted by
884 the yellow arrow and circle, from the conservative mixing line (the dashed line and
885 grey band $\pm 2\sigma$) between NADW and AABW during the N-S Atlantic water transport.

886 Additional Ba inputs (e.g. hydrothermal input) may be responsible for the apparent non-
887 conservative behavior. The Ba compositions of NADW ([Ba] \approx 51 nmol/kg; $\delta^{138/134}\text{Ba}$
888 \approx +0.45‰) and AABW ([Ba] \approx 103 nmol/kg; $\delta^{138/134}\text{Ba}$ \approx +0.25‰) have been assessed
889 by Hsieh and Henderson (2017) and Bates et al. (2017). Compiled data are from Horner
890 et al. (2015), Bates et al. (2017), Hsieh and Henderson (2017), Bridgestock et al. (2018)
891 and Hemsing et al., (2018).

892

893 **Figure 2.** Location of MOR hydrothermal vent fields and sampling years in this study.

894

895 **Figure 3.** Ba, Mg and SO₄ concentrations and Ba isotope compositions for MOR
896 hydrothermal vent fluids from MAR (Rainbow 36°N and TAG 26°N), EPR (9-10°N
897 and 13°N) and JdFR (MEF and ASHES) vent systems. **(a)** Hydrothermal vent fluid
898 [SO₄] versus [Mg] (dashed line represents conservative mixing between vent fluids and
899 seawater). **(b)** Plot of vent fluid [Ba] versus [SO₄], and the expected curve for barite
900 saturation ($\Omega_{\text{barite}} = 1$) at deep-water T-P condition (1°C and 500 bar), demonstrating
901 that many samples are super-saturated for barite. The circles show the focused-flow
902 fluids and the triangles show the diffuse-flow samples. The closed symbols show the
903 dregs corrected fluid Ba compositions (equation 1) and the open symbols show all the
904 non-corrected data. Seawater and vent fluid conservative mixing is illustrated in dashed
905 lines. Removal of Ba by barite precipitation during mixing with seawater is highlighted
906 by the purple arrow. **(c)** Plot of Ba isotopes and Ba/Mg ratios for vent fluids (both dregs
907 corrected and non-corrected; Section 4.2) indicating Ba isotope fractionation during
908 mixing of vent fluids and seawater and resulting barite precipitation. The data show the
909 largest range of $\delta^{138/134}\text{Ba}$ (-0.26 ~ +0.91 ‰) so far seen in any marine environment.
910 Seawater Ba concentration and isotope data are the average values (between 2000 and

911 3000m) from the North Atlantic (BATS, Hsieh and Henderson, 2017) and North Pacific
912 (SAFe, Geyman et al., 2019).

913

914 **Figure 4. (a)** Comparisons of vent fluid $\delta^{138/134}\text{Ba}$ values between different vent fields.
915 The open red diamonds are the measured values and the solid red diamonds are the
916 dregs corrected values. The black squares are the estimates of endmember vent fluid in
917 each field. **(b)** Comparisons of $\delta^{138/134}\text{Ba}$ values in marine systems: seawater (Horner
918 et al., 2015; Hsieh and Henderson, 2017; Bates et al., 2017; Horner et al., 2017;
919 Bridgestock et al., 2018; Hemsing et al., 2018; Geyman et al., 2019; Cao et al., 2020),
920 rivers (Cao et al., 2016; Hsieh and Henderson, 2017; Gou et al., 2020), MORBs and
921 AOC (Nielsen et al., 2018; Nielsen et al., 2020), pelagic sediments (Bridgestock et al.,
922 2018; Crockford et al., 2019; Nielsen et al., 2020), and hydrothermal vent fluids (this
923 study). The hydrothermal vent fluid data show the largest range of $\delta^{138/134}\text{Ba}$ (-0.26 ~
924 +0.91 ‰) so far seen in marine environments. The effective hydrothermal input
925 $\delta^{138/134}\text{Ba}$ ($+1.7 \pm 0.7\text{‰}$, red square) is extrapolated by barite saturation and Ba isotope
926 fractionation models (Discussion 4.4).

927

928 **Figure 5.** Barium versus magnesium in the (a) Rainbow, (b) MEF, (c) EPR 9-10°N,
929 and (d) EPR 13°N hydrothermal vent fluids. The blue open circles show the dregs
930 corrected Ba concentrations ($[\text{Ba}]_{\text{corr}}$) and the red closed circles show the $\delta^{138/134}\text{Ba}$ -
931 derived hypothetical Ba concentration ($[\text{Ba}]_{\text{corr}}^*$) prior to barite precipitation. The
932 dashed lines show the linear regressions through the $[\text{Ba}]$ and $[\text{Mg}]$ data, which are used
933 to extrapolate the endmember fluid $[\text{Ba}]$ at the intercept of zero Mg ($\pm 1\text{SD}$).

934

935 **Figure 6.** Ba isotopes and concentrations in the Rainbow, EPR 9-10°N, EPR 13°N and
936 MEF hydrothermal vent fluids with seawater mixing, Rayleigh fractionation and barite
937 saturation models. **(a-d)** The data of Ba isotopes and 1/[Ba] show increased $\delta^{138/134}\text{Ba}$
938 as [Ba] in vent fluids decreases. A Rayleigh fractionation model with a fractionation
939 factor $\Delta^{138/134}\text{Ba}_{\text{hyd-barite-fluid}} = -0.35 \pm 0.10 \text{ ‰}$ (orange and blue lines) is applied to fit the
940 data. The initial endmember fluid compositions are taken from Table 3. The closed and
941 open circles are the dregs corrected and uncorrected fluid Ba compositions respectively.
942 Samples outside the range of the model trajectory are labeled individually. They are
943 likely to be affected by phase separation (PS), evidenced by low [Cl] and [Ca] (Table
944 S1), or diffuse-flow (DF) in a more complex circulation environment. Foustoukos et al.
945 (2009) have also noticed that Smoke & Mirrors (S&M) may have a different circulation
946 environment from other focused-flow vents in the MEF vent field. **(e-h)** Extrapolation
947 of curves in (a-d) to the [Ba] values at the end point of hydrothermal plumes during
948 mixing with seawater. Barite saturation values ($\Omega_{\text{barite}} = 1$) are shown by green vertical
949 lines. Once [Ba] becomes under-saturated ($< 0.2 \text{ } \mu\text{mol/kg}$, $\Omega_{\text{barite}} < 1$), remaining Ba in
950 the plumes starts to mix conservatively with seawater, as indicated by the black arrow.
951 The effective hydrothermal Ba isotope compositions are labeled in green. Seawater Ba
952 data are from Hsieh and Henderson (2017) and Geyman et al. (2019). NA and NP stand
953 for the North Atlantic and the North Pacific seawaters respectively. The brown bands
954 refer to the range of $\delta^{138/134}\text{Ba}$ values in MORBs (+0.02 to +0.15‰; Nielsen et al., 2018).
955

956 **Figure 7.** Estimated hydrothermal Ba input in the deep Atlantic Ocean. **(a)** Three
957 endmembers mixing model. The red square shows the hydrothermal value with its
958 uncertainty ([Ba] $\approx 200 \text{ nmol/kg}$; $\delta^{138/134}\text{Ba} = +1.7 \pm 0.7\text{‰}$), and the blue and green
959 squares show the compositions of NADW ([Ba] $\approx 51 \text{ nmol/kg}$; $\delta^{138/134}\text{Ba} \approx +0.45\text{‰}$)

960 and AABW ($[Ba] \approx 103$ nmol/kg; $\delta^{138/134}Ba \approx +0.25\%$) respectively (Hsieh and
961 Henderson, 2017; Bates et al., 2017). The yellow square shows the mixed seawater
962 composition (SW_{SA}) between 2000 and 3000 m depth from the South Atlantic ($[Ba] \approx$
963 78 nmol/kg; $\delta^{138/134}Ba \approx +0.39\%$) (Horner et al., 2015; Hsieh and Henderson, 2017).
964 Dashed mixing lines between the hydrothermal Ba and deep water endmembers are
965 labeled with open circles to indicate the fractions of hydrothermal Ba input (F_{Ba_hyd}) in
966 the deep water Ba (0-100%). The non-hydrothermal Ba fractions between NADW and
967 AABW are labeled with crosses. As the uncertainty of the hydrothermal $\delta^{138/134}Ba$
968 composition is large, models are calculated against the average value (orange dashed
969 lines) as well as the high and low ends of the values (grey dashed lines). **(b)** The impact
970 of hydrothermal Ba input on the distribution of deep-water $[Ba]$ and $\delta^{138/134}Ba$ (Fig. 1).
971 The dashed lines show the fraction of hydrothermal Ba input (F_{Ba_hyd}) in the deep water
972 Ba (0-10%). The fraction values on display are calculated against the average
973 hydrothermal $\delta^{138/134}Ba$ (+1.7%). The original data of the yellow square shown in (a)
974 is highlighted in the yellow area.

975

976 **Figure 8.** Relationship between seawater SO_4 concentrations and the input
977 compositions of effective hydrothermal Ba ($[Ba]_{hyd}$ and $\delta^{138/134}Ba_{hyd}$) in the ocean. The
978 yellow curve shows $[Ba]_{hyd}$, based on the barite saturation model ($\Omega_{barite} = 1$) at deep-
979 water T-P condition (1°C and 500bar) (Monnin, 1999). The blue curve shows
980 $\delta^{138/134}Ba_{hyd}$ with uncertainties (the grey curves), based on a fractionation factor
981 ($\Delta^{138/134}Ba_{hyd-barite-fluid} = -0.35 \pm 0.10$ ‰) and $[Ba]_{hyd}$ in the Ba isotope fractionation
982 model. For illustrative purposes, the initial composition for the fractionation is taken
983 from the average values of endmember fluids (Table 3) as a generic composition ($[Ba]$
984 $= 42$ μ mol/kg and $\delta^{138/134}Ba = -0.07$ ‰).

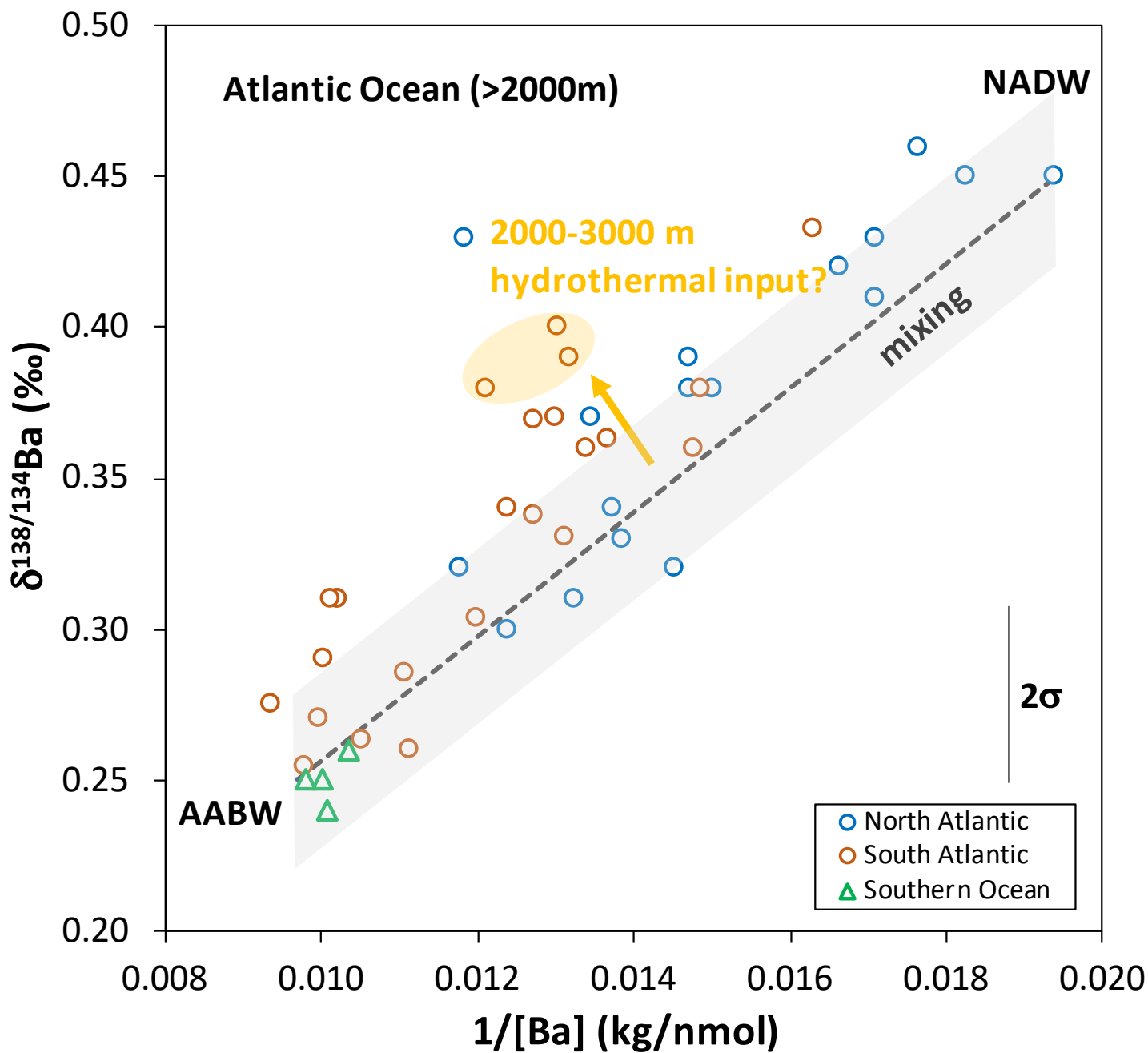
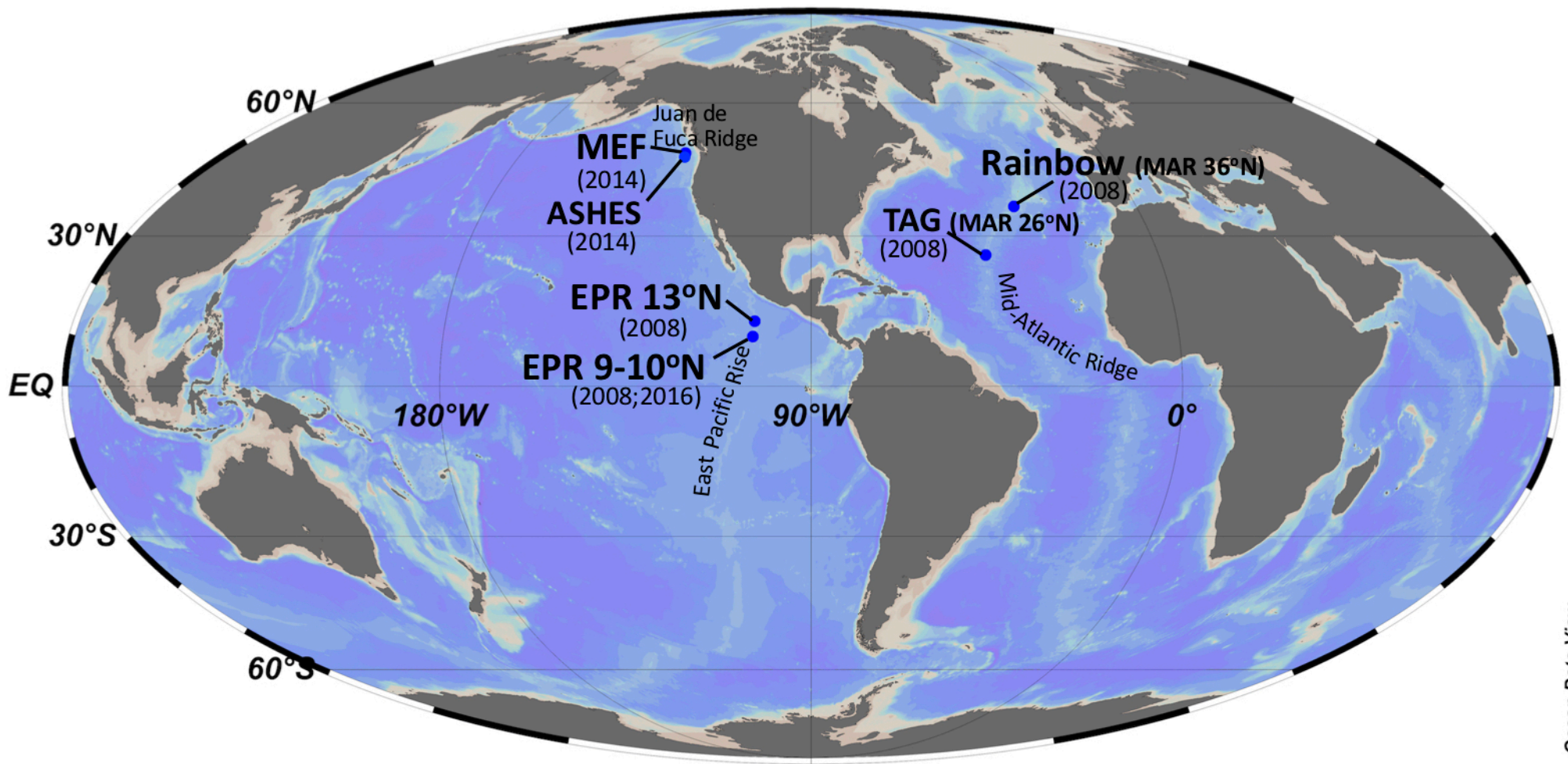


Figure 1



Ocean Data View

Figure 2

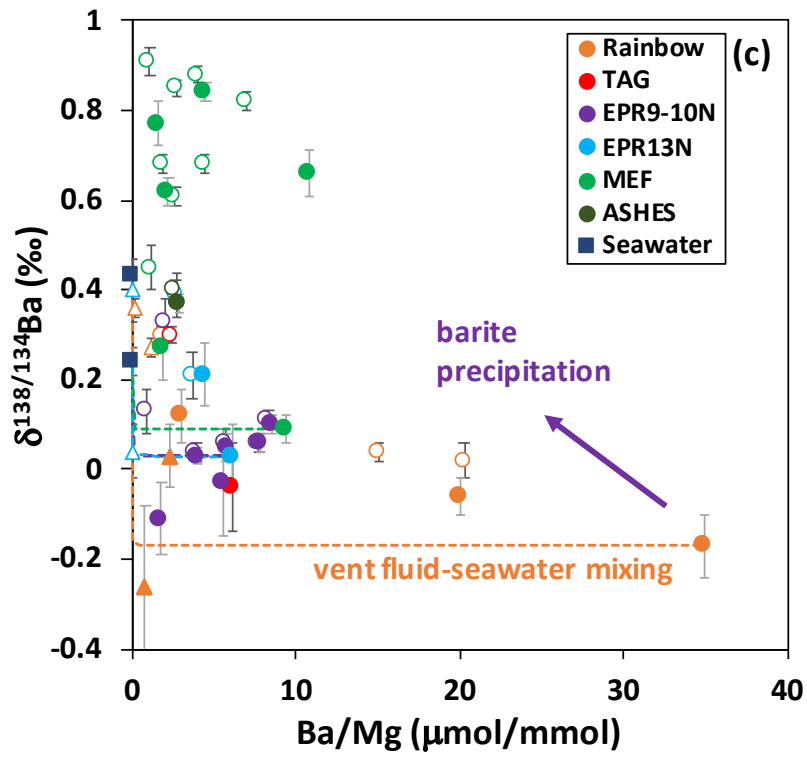
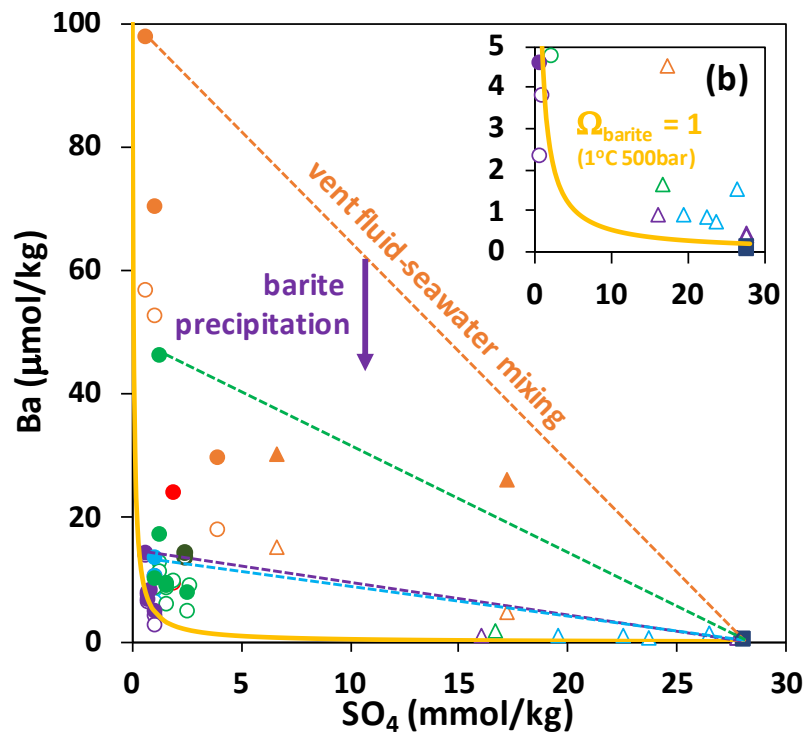
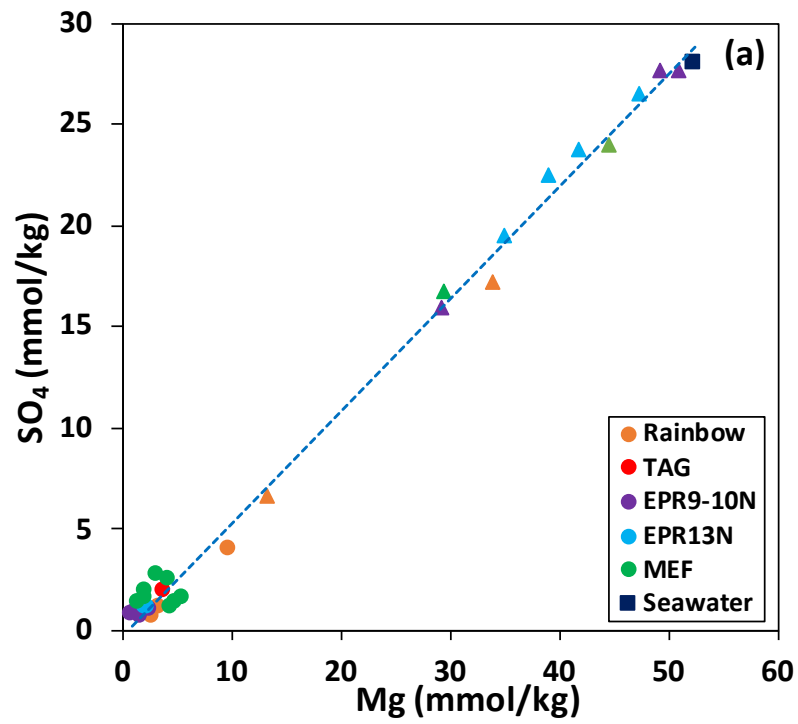
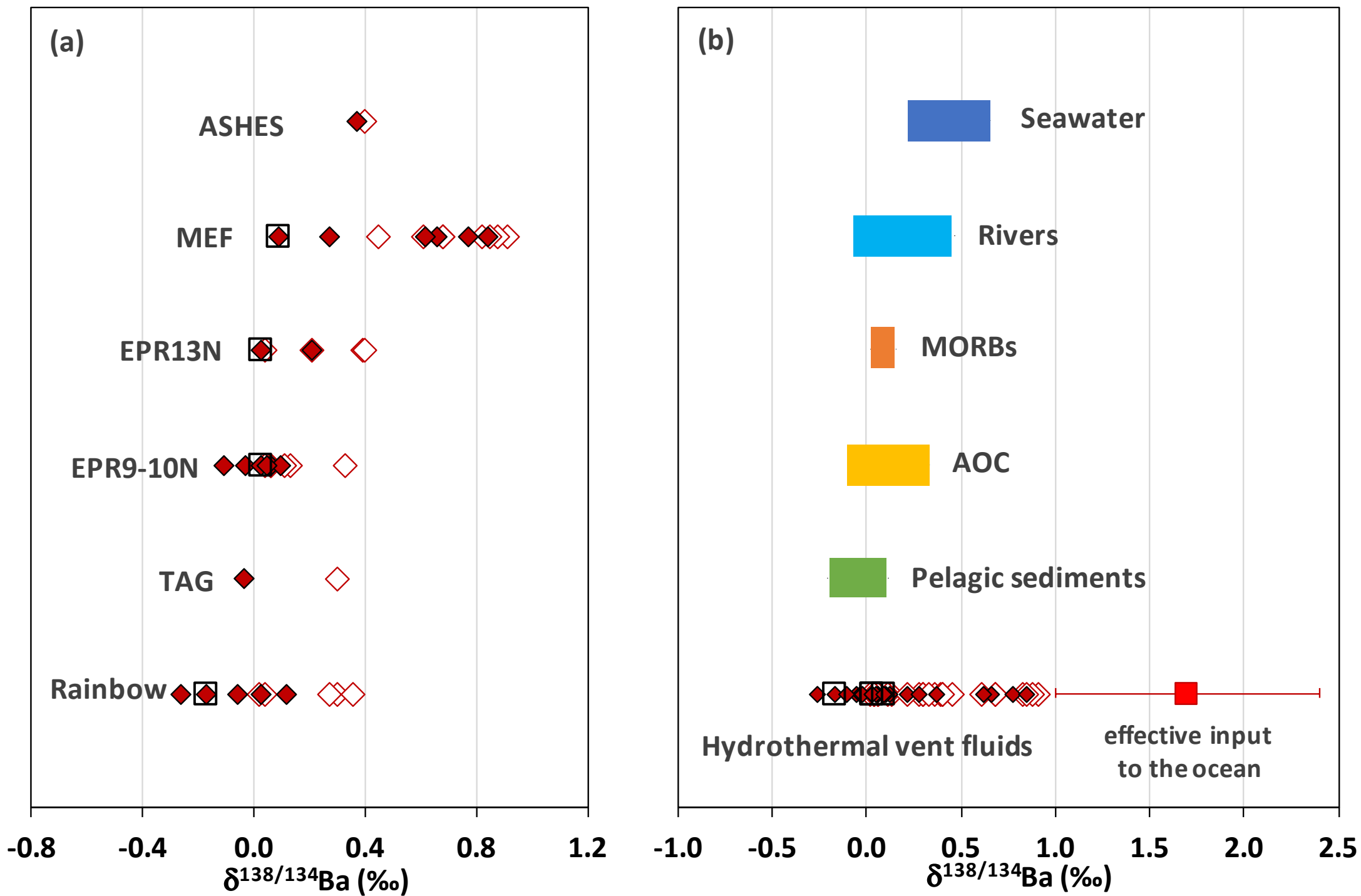


Figure 3



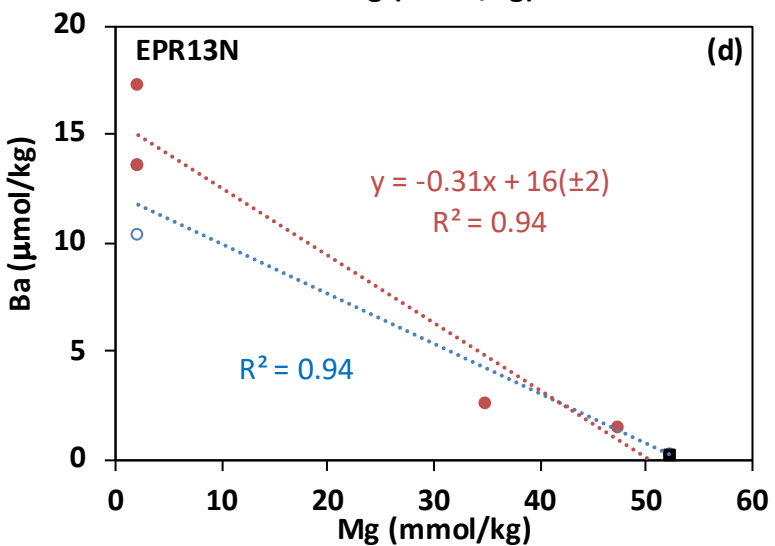
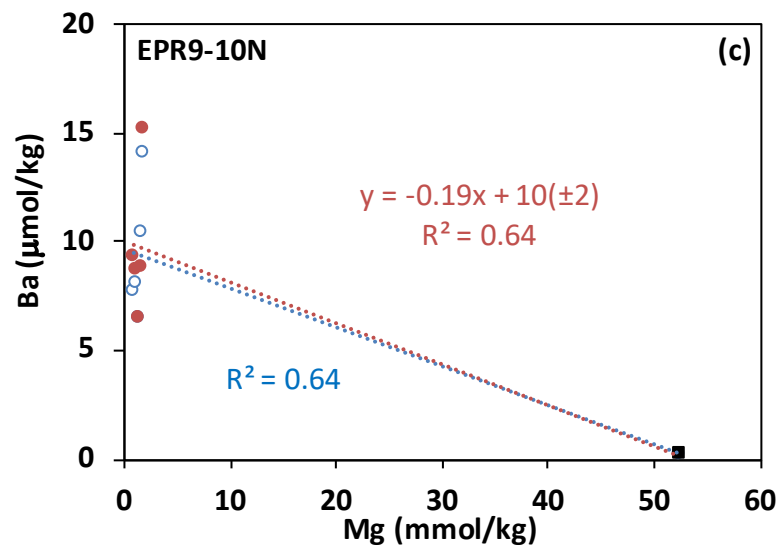
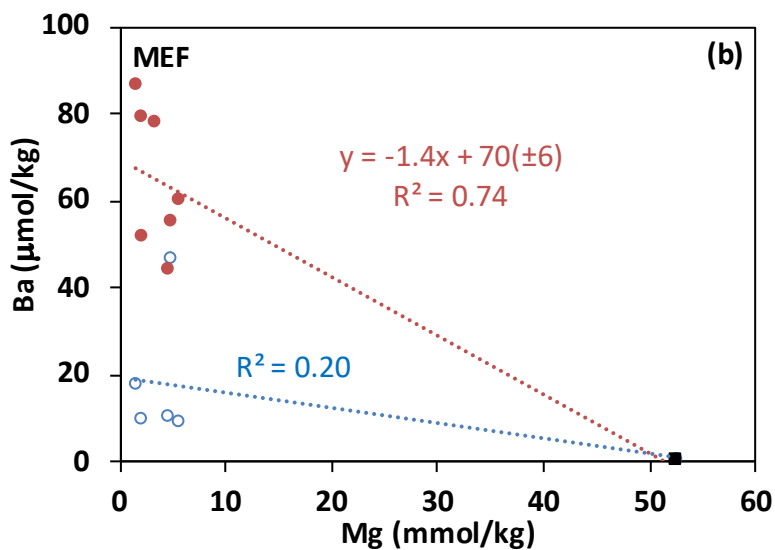
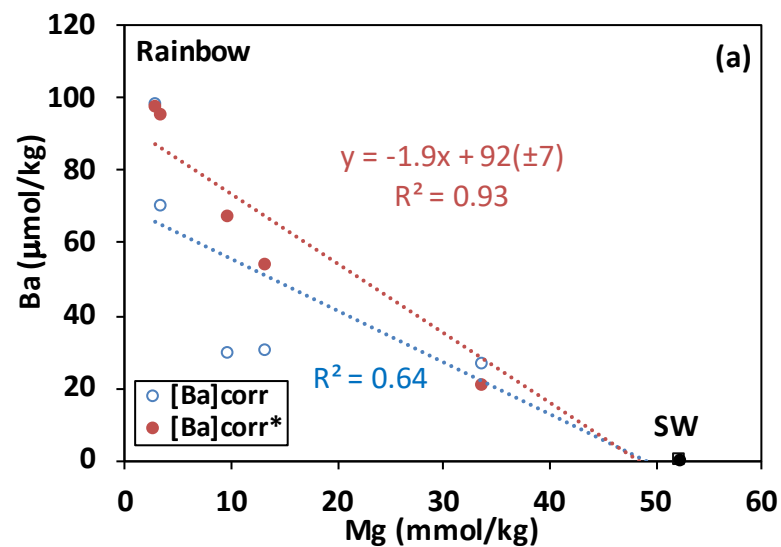


Figure 5

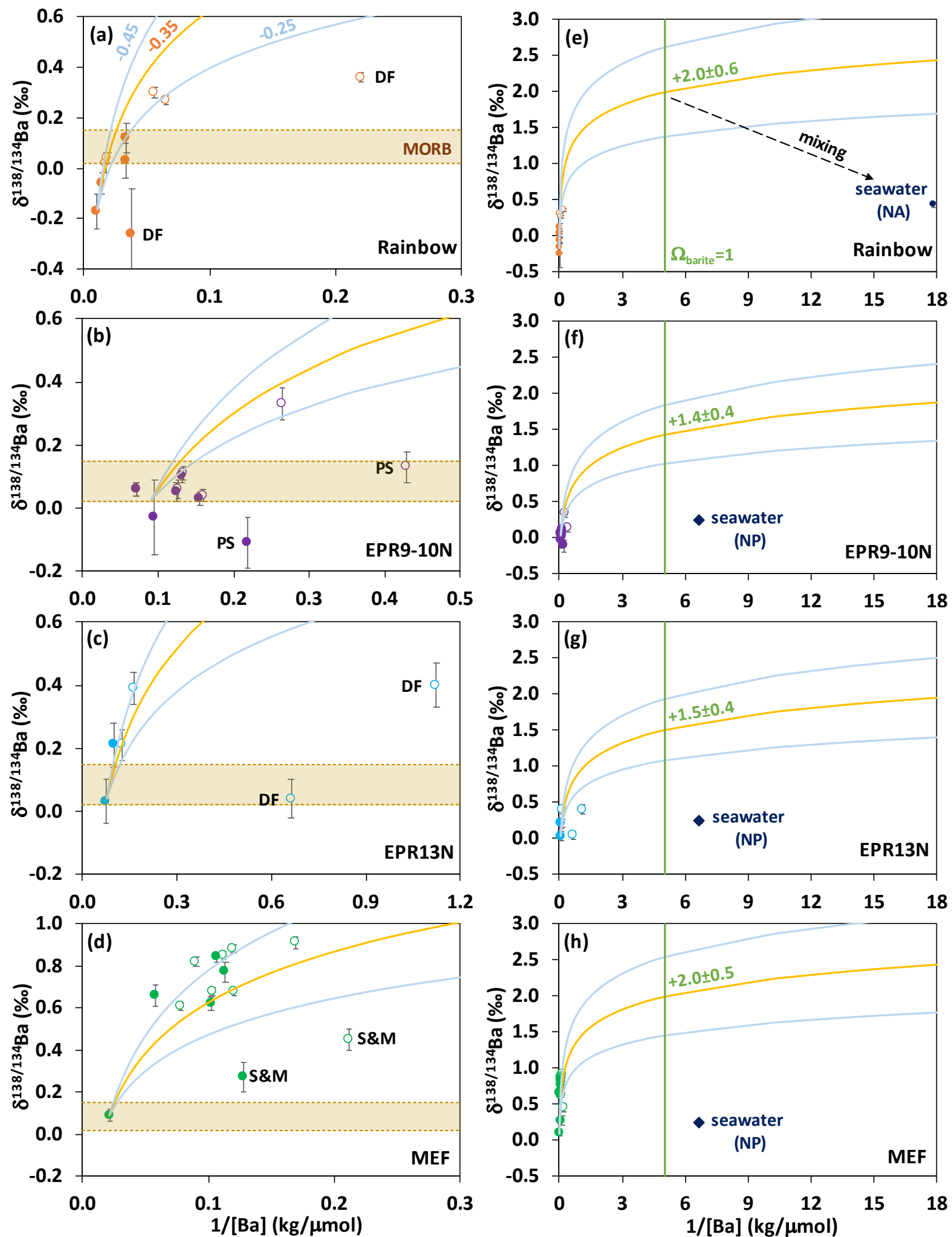


Figure 6

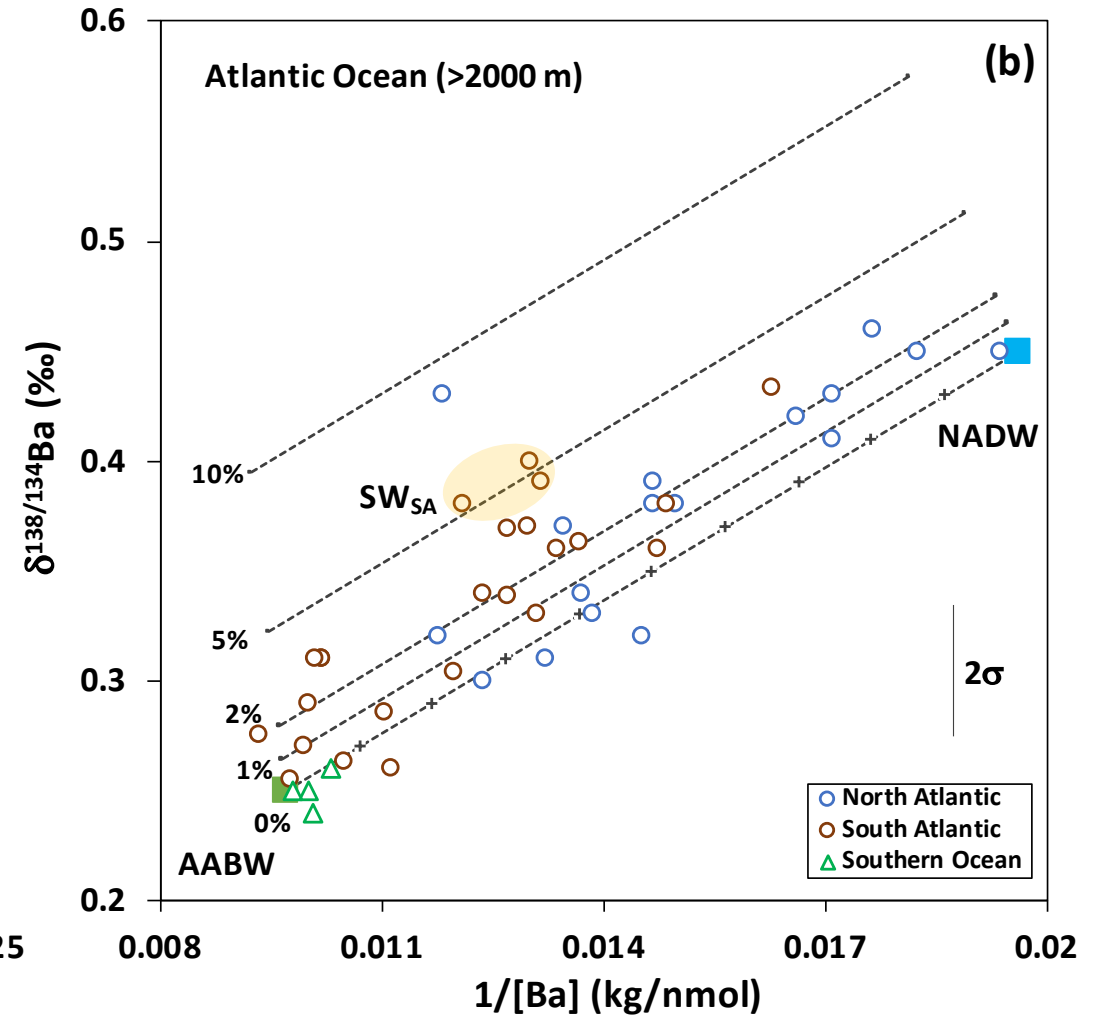
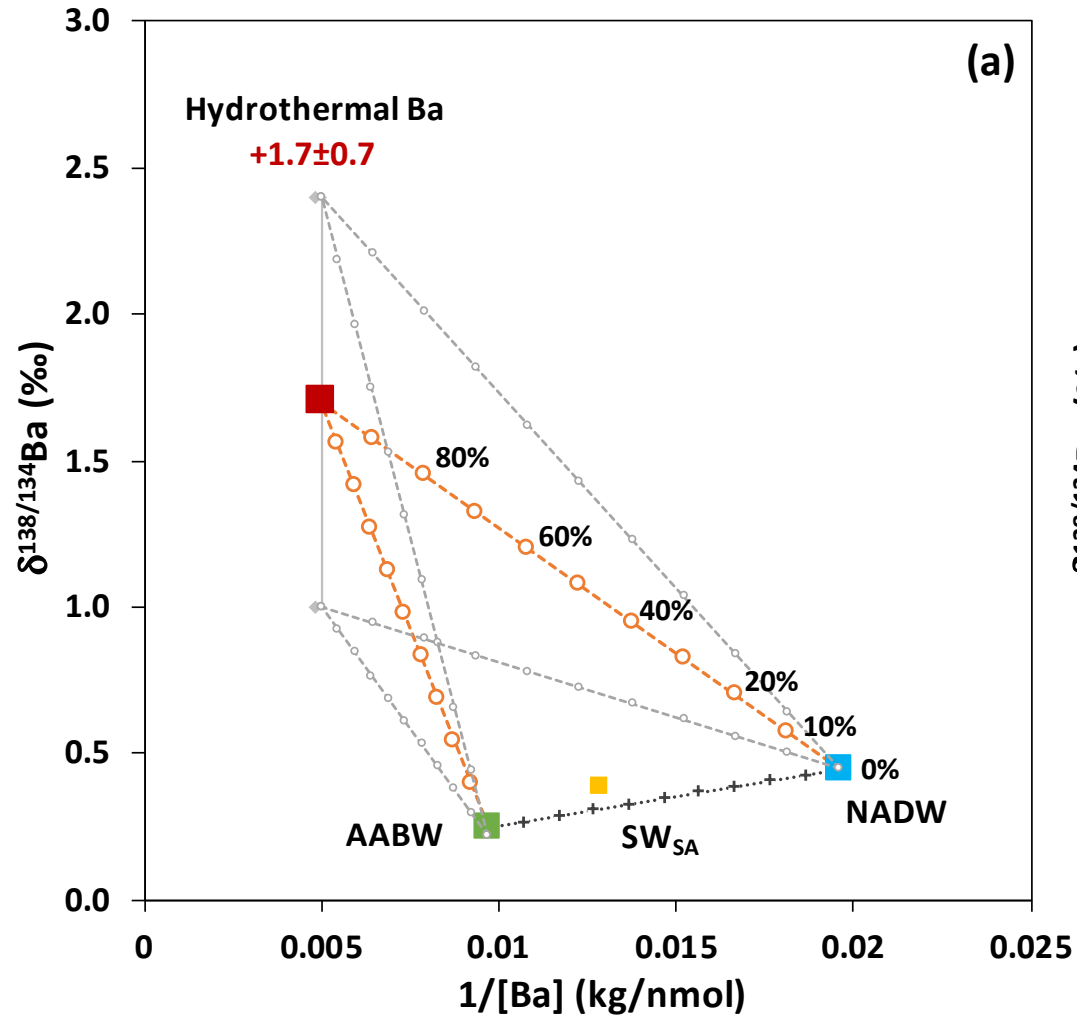


Figure 7

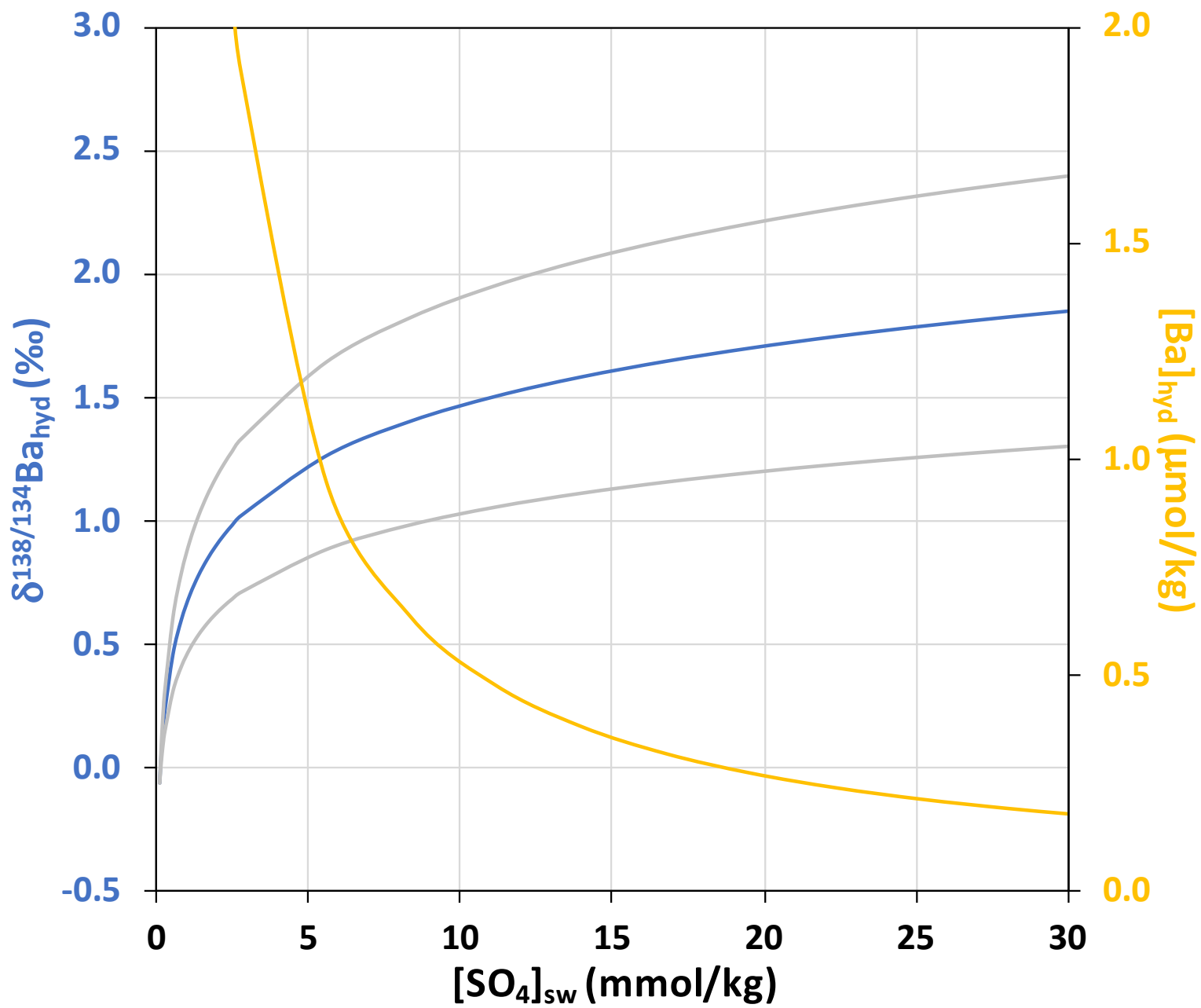


Figure 8

Table 1 Vent fluid and particle (dregs) sample information, temperature, Mg, SO₄ and Ba concentrations and Ba isotope composition.

Vent	Type ^a	Sample ID	Temp (°C)	Mg (mmol/kg)	SO ₄ (mmol/kg)	Ba-uncorr ^b δ ^{138/134} (μmol/kg)	Ba ±2S.D. ^j uncorr	Ba-dregs ^c (μmol/kg)	Ba-corr ^e (μmol/kg)	δ ^{138/134} corr ^e	Ba ±2S.D. corr ^e	
Rainbow (MAR 36°N) (2008) (36.23°N, 33.90°W)^f												
Guillaume, X4	FF	352-IGT4	354	2.8	0.66	56.7	0.02	0.04	41.2	97.9	-0.17	0.07
Regner	FF	353-IGT2	323	9.8	4.02	17.8	0.30	0.02	11.8	29.6	0.12	0.06
CMSP&P	FF	354-IGT3	365	3.5	1.15	52.6	0.04	0.02	17.6	70.2	-0.06	0.04
Ecurie	DF	354-IGT4	66	33.8	17.2	4.54	0.36	0.02	21.7	26.2	-0.26	0.18
Ecurie	DF	354-IGT8	128	13.2	6.61	15.3	0.27	0.02	15.0	30.3	0.03	0.07
TAG (MAR 26°N) (2008) (26.14°N, 44.83°W)												
TAG	FF	363-IGT5	366	3.9	2.0	9.22	0.30	0.02	14.8	24.0	-0.04	0.10
EPR9-10°N (2008) (9.83°N, 104.29°W)^g												
Bio-9	FF	4386-IGT6	330	1.9	1.1	3.78	0.33	0.05	6.68	10.5	-0.03	0.12
Tica	DF	4388-IGT5	25	29.3	16.0	0.89 ^b						
Ty-lo	FF	4393-IGT6	304	2.6	1.07	2.33	0.13	0.05	2.26	4.59	-0.11	0.08
Crab-Spa	DF	4394-IGT6	23	49.3	27.7	0.46 ^b						
Ty-lo	DF	4397-IGT5	13	51	27.7	0.43 ^b						
EPR9-10°N (2016) (9.83°N, 104.29°W)												
Bio-9	FF	4837-IGTD	374	1.8	0.7	13.9	0.06	0.02	0.17 ^d	14.1	0.06	0.02
Bio-9	FF	4838-IGTB	373	1.6	0.8	6.27	0.04	0.02	0.17 ^d	6.44	0.03	0.02
Pvent	FF	4838-2-6	363	0.9	0.8	7.47	0.11	0.02	0.17 ^d	7.64	0.10	0.02
Pvent	FF	4841-2-4	354	1.4	0.9	7.92	0.06	0.03	0.16 ^d	8.08	0.05	0.03
EPR13°N (2008) (12.83°N, 103.95°W)^{g,h}												
Grand Bonum	FF	4389-IGT5	350	2.2	1.1	8.02	0.21	0.05	5.35	13.4	0.03	0.07
Dorian	DF	4391-MG		39.1	22.5	0.88 ^b						
Dorian	FF	4392-IGT5	344	2.3	1.1	6.17	0.39	0.05	4.02	10.2	0.21	0.07
Jumeaux	DF	4392-MG	148	34.9	19.5	0.89	0.40	0.07				
Ph05	DF	4392-IGT6	148	41.8	23.7	0.72 ^b						
Actinoir	DF	4391-MW	74	47.3	26.5	1.51	0.04	0.06				
MEF (2014) (47.95°N, 129.10°W)^{g,i}												
Bastille	FF	4743-C	321	5.6	1.63	5.92	0.91	0.03	2.90	8.82	0.77	0.05
Bastille	FF	4743-2	317	4.9	1.34	12.8	0.61	0.02	33.3	46.1	0.09	0.03
Lobo	FF	4743-D	333	1.6	1.36	11.1	0.82	0.02	6.20	17.3	0.66	0.05
TP	FF	4743-E	334	2.1	1.59	8.36	0.88	0.02	1.00	9.36	0.84	0.02
Lobo	FF	4744-1	335	3.3	2.7	8.93	0.85	0.02				
Dante	FF	4744-2	329	2.2	1.91	9.72	0.68	0.02				
Sully Flange	DF	4743-4	267	29.4	16.7	1.65 ^b						
Puffer	FF	4743-5	280	4.5	1.14	8.32	0.68	0.02	1.50	9.82	0.62	0.03
S and M	FF	4743-6	291	4.2	2.57	4.73	0.45	0.05	3.10	7.83	0.27	0.07
ASHES (2014) (45.93°N, 130.01°W)^{g,i}												
Inferno	FF	4741-D	299	5	2.47	13.2	0.40	0.02	1.10	14.3	0.37	0.02
Seawater												
N Atlantic BATS (2000-3000m, n=3) (Hsieh and Henderson, 2017)						0.06	0.43	0.04				
N Pacific SAFe (2000-3000m, n=5) (Geyman et al., 2019)						0.15	0.24	0.03				

^aVent type FF: focused-flow; DF: diffuse-flow. ^b[Ba] fluid data analyzed by Quad-ICP-MS. ^cDregs [Ba] is normalized to the volume of samplers. ^dDregs [Ba] data analyzed by ID-TIMS. ^eBa data are corrected for dregs Ba removal and isotope fractionation (Discussion 4.2).

^{f,g,h,i}More sample information and other data are available in ^fSeyfried et al. (2011), ^gScheuermann et al., (2018), ^hPester et al. (2011) and ⁱSyverson et al. (2017). ^jThe external reproducibility is 0.02 (±2SD).

Table 2 Vent fluid and particle (dregs) Ba concentration, isotope composition and fractionation factor.

Sample		Fluids-uncorr		Dregs		Fluids-corr		dregs-fluid
Vent	ID	Ba	$\delta^{138/134}\text{Ba}$	Ba	$\delta^{138/134}\text{Ba}$	Ba	$\delta^{138/134}\text{Ba}$	$\Delta^{138/134}\text{Ba}$
		($\mu\text{mol/kg}$)	$\pm 2\text{S.D.}$	($\mu\text{mol/kg}$)	$\pm 2\text{S.D.}$	($\mu\text{mol/kg}$)	$\pm 2\text{S.D.}$	$\pm 2\text{S.D.}$
MEF (2014)								
Bastille	4743-2	12.8	0.61 ± 0.02	33.3	-0.11 ± 0.02	46.1	0.09 ± 0.03	-0.40 ± 0.03
ASHES (2014)								
Inferno	4741-D	13.2	0.40 ± 0.02	1.1	0.08 ± 0.08	14.3	0.37 ± 0.02	-0.30 ± 0.08
Mean ($\pm 2\text{SE}$)								-0.35 ± 0.10

Table 3 Summary of calculated Ba compositions in endmember fluids.

Hydrothermal systems	Endmember fluids		
	Ba ($\mu\text{mol/kg}$)	Ba* ($\mu\text{mol/kg}$)	$\delta^{138/134}\text{Ba}$
MAR Rainbow (36°N)	98	92 \pm 7	-0.17
EPR 9-10°N ^a	11	10 \pm 2	0.03
EPR 13°N	13	16 \pm 2	0.03
JdFR MEF	46	70 \pm 6	0.09

^aValues based on the mean of three highest [Ba] samples

*Estimates based on the extrapolations at zero Mg (Fig. 5)

**Barium isotopes in mid-ocean ridge hydrothermal vent fluids: a
source of isotopically heavy Ba to the ocean**

Supplementary material

**Yu-Te Hsieh^{a,*}, Luke Bridgestock^a, Peter P. Scheuermann^b, William E. Seyfried Jr.^b,
and Gideon M. Henderson^a**

^aDepartment of Earth Sciences, University of Oxford, UK

^bDepartment of Earth and Environmental Sciences, University of Minnesota, USA

*Corresponding author: yu-te.hsieh@earth.ox.ac.uk

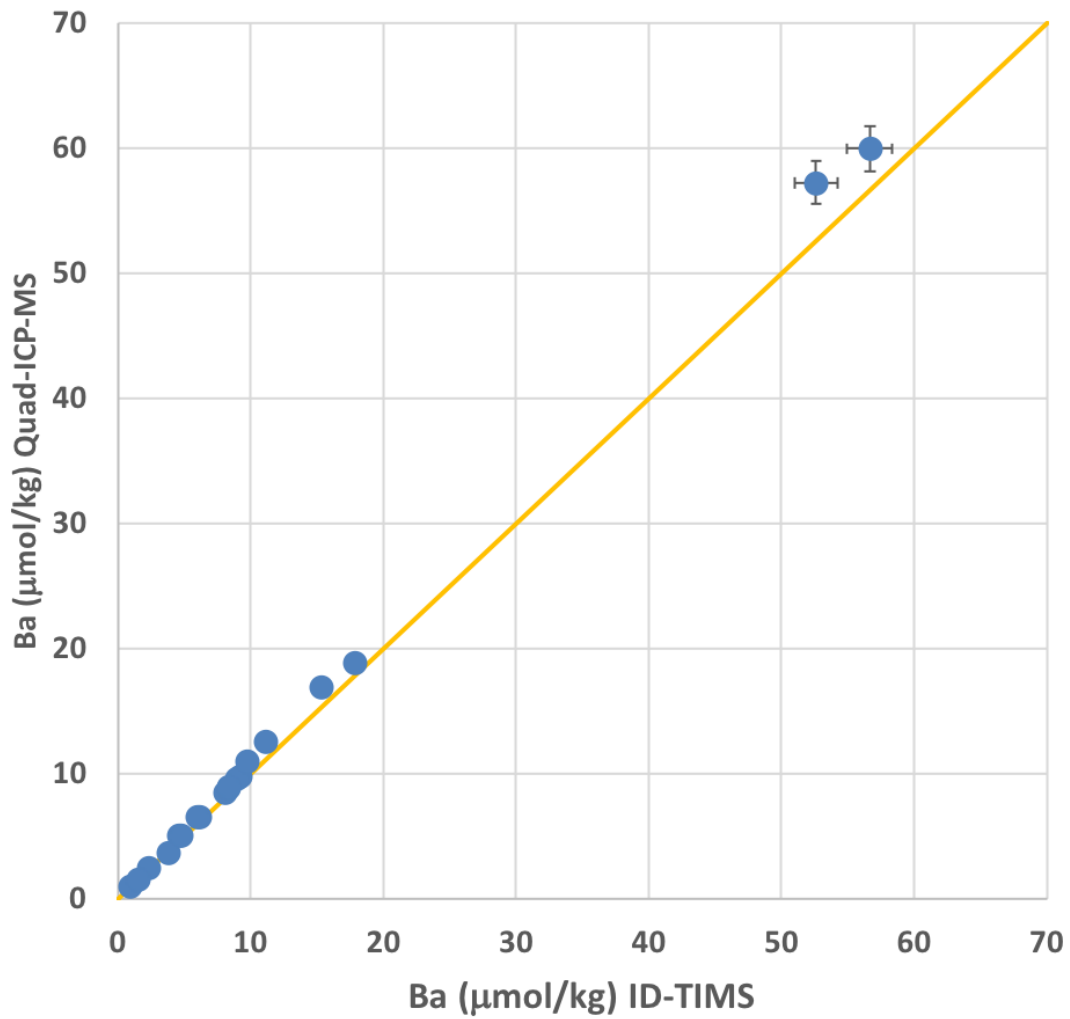


Figure S1. Comparisons of hydrothermal vent fluid Ba concentration data by Quad-ICP-MS and ID-TIMS. The data are generally agreed between the two methods within 1-11%. The offset may reflect the sample dilution and matrix effects between the Quad-ICP-MS and ID-TIMS analyses. The orange line is 1:1, and the error bars are $\pm 3\%$ (1SD).

S1. Calculating dregs corrected vent fluid $\delta^{138/134}\text{Ba}$ and $\Delta^{138/134}\text{Ba}$ values

To calculate the dregs corrected vent fluid Ba isotopic compositions, two dregs samples from MEF (4743-2) and ASHES (4741-D) were analyzed for Ba isotopes to reconstruct the corrected fluid $\delta^{138/134}\text{Ba}$ and to calculate the isotope effect $\Delta^{138/134}\text{Ba}_{\text{dregs-fluid}}$ on the samples. The dregs corrected fluid Ba isotopic composition ($\delta^{138/134}\text{Ba}_{\text{corr}}$) is calculated as:

$$\delta^{138/134}\text{Ba}_{\text{corr}} = f \cdot \delta^{138/134}\text{Ba}_{\text{fluid}} + (1-f) \cdot \delta^{138/134}\text{Ba}_{\text{dregs}} \quad (\text{S1})$$

$$f = [\text{Ba}]_{\text{fluid}} / [\text{Ba}]_{\text{corr}} \quad (\text{S2})$$

where f is the fraction of dissolved Ba in the total fluid Ba and $(1-f)$ is the fraction of dregs Ba. The instantaneous isotope fractionation factor between fluid and dregs is calculated using the Rayleigh isotope fractionation model:

$$\Delta^{138/134}\text{Ba}_{\text{dregs-fluid}} = (\delta^{138/134}\text{Ba}_{\text{fluid}} - \delta^{138/134}\text{Ba}_{\text{corr}}) / \ln(f) \quad (\text{S3})$$

The dregs corrected fluid $[\text{Ba}]$ ranges from 6.44 to 97.9 $\mu\text{mol/kg}$ when the dregs fraction is recovered (Table 1), and the fraction of dissolved Ba (f) varies between 0.17 and 0.98 in the vent fluids. For two samples MEF and ASHES, their $\delta^{138/134}\text{Ba}_{\text{dregs}}$ and $\delta^{138/134}\text{Ba}_{\text{fluid}}$ compositions and the dissolved Ba fraction f were used to calculate the isotope fractionation factor $\Delta^{138/134}\text{Ba}_{\text{dregs-fluid}}$ between dregs and fluids. The calculated $\Delta^{138/134}\text{Ba}_{\text{dregs-fluid}}$ values are $-0.40 \pm 0.02 \text{‰}$ (4743-2) and $-0.30 \pm 0.08 \text{‰}$ (4741-D), with an average value of $-0.35 \pm 0.10 \text{‰}$ (2SE, $n=2$), considering the uncertainty of $[\text{Ba}]$ and $\delta^{138/134}\text{Ba}$ values (Table 2).

As vent fluids generally have a much higher Ba concentration ($[\text{Ba}] > 10 \mu\text{mol/kg}$) than seawater, the Ba contribution from the seawater component in this calculation is mostly negligible. For example, using Mg as a conservative tracer to estimate the component of seawater in vent fluids and assuming that seawater $[\text{Ba}] = 0.1 \mu\text{mol/kg}$, the estimate of seawater contribution is $< 0.1\%$ of total Ba in all of the focused-flow samples of this study.

For the diffuse-flow samples, due to a high degree of seawater entrainment, seawater Ba contribution varies from 0.1 to 25%, which may affect the corrections of vent fluid Ba isotope composition. In this study, the majority of diffuse-flow data is reported as uncorrected only due to the absence of dregs. For future studies of Ba in diffuse-flow vent fluids, the seawater component should be considered.

S2. Using $\delta^{138/134}\text{Ba}$ values to calculate the corrected Ba concentrations ($[\text{Ba}]_{\text{corr}^*}$) prior to barite precipitation in vent fluids

Even after the dregs correction (see above), the corrected fluid Ba concentrations still show non-conservative behavior (Fig. 3b), which implies that either some barite precipitation has occurred in the subsurface prior to venting of the fluids or there is a low recovery of dregs in the samplers. Although it is not possible to separate the Ba loss between these two processes, when the endmember vent fluid $\delta^{138/134}\text{Ba}$ values can be obtained, Ba isotopes may provide a new approach to calculate the total loss of Ba and the hypothetical concentration of the corrected Ba ($[\text{Ba}]_{\text{corr}^*}$) in vent fluids prior to barite precipitation using a Rayleigh isotope fractionation model:

$$[\text{Ba}]_{\text{corr}^*} = [\text{Ba}]_{\text{fluid}} / \exp[(\delta^{138/134}\text{Ba}_{\text{fluid}} - \delta^{138/134}\text{Ba}_{\text{corr}^*}) / \Delta^{138/134}\text{Ba}_{\text{hyd-barite-fluid}}] \quad (\text{S4})$$

where $[\text{Ba}]_{\text{fluid}}$ and $\delta^{138/134}\text{Ba}_{\text{fluid}}$ are the measured Ba concentrations and Ba isotope compositions in vent fluids (before dregs correction); $\Delta^{138/134}\text{Ba}_{\text{hyd-barite-fluid}}$ is the hydrothermal barite isotope fractionation factor ($\Delta^{138/134}\text{Ba}_{\text{hyd-barite-fluid}} = -0.35 \pm 0.10 \text{ ‰}$); and $\delta^{138/134}\text{Ba}_{\text{corr}^*}$ is the corrected Ba isotope composition prior to barite precipitation in vent fluids. Without barite precipitation, the $\delta^{138/134}\text{Ba}_{\text{corr}^*}$ values should be a result of simple mixing between the endmember vent fluids and seawater (Fig. 3c). As mentioned in supplementary material S1, the endmember fluid Ba concentrations are generally several orders of magnitude higher than seawater, Ba contribution from seawater is $< 0.1\%$ of total

Ba in most of the mixed vent fluids in this study. Therefore, the $\delta^{138/134}\text{Ba}_{\text{corr}}^*$ values can be assumed to be the same as the endmember fluid $\delta^{138/134}\text{Ba}$ values in each vent field. In this study, the agreement between the endmember fluid and source rock $\delta^{138/134}\text{Ba}$ values implies that these estimates of the endmember fluid $\delta^{138/134}\text{Ba}$ values in Table 3 are not unreasonable. The recovery of Ba after the dregs correction can also be estimated by comparing the dregs corrected $[\text{Ba}]_{\text{corr}}$ (equation 1) and the $\delta^{138/134}\text{Ba}$ -derived $[\text{Ba}]_{\text{corr}}^*$ values.

The estimates of $[\text{Ba}]_{\text{corr}}^*$ values and the recovery of Ba after the dregs correction are reported in Table S1 and Fig. S2 for comparison. The recovery of Ba varies from 12 to 130% after the dregs correction, with an average of 71%. It is noted that the vent fluids from MEF and Rainbow seem to have slightly poor Ba recovery (Fig. S2). This calculation has only been applied to the fluid samples that are available with Ba isotope data and the endmember $\delta^{138/134}\text{Ba}$ values in Rainbow, EPR and MEF vent fields, except for two samples (Ty-lo 4939-IGT6 and S&M 4743-6) as the endmember $\delta^{138/134}\text{Ba}$ values are not applicable (discussed in Section 4.4 and Fig. 5).

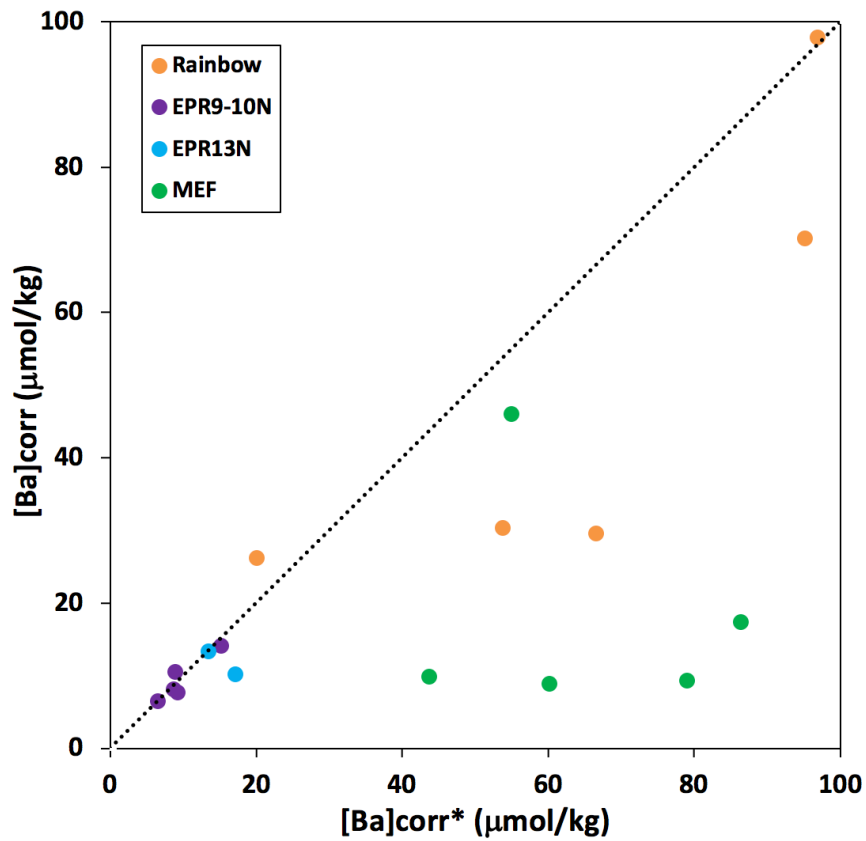


Figure S2. Comparisons of the corrected Ba concentrations in vent fluids between the dregs correction ($[Ba]_{corr}$) and the $\delta^{138/134}Ba$ -derived hypothetical Ba concentration ($[Ba]_{corr}^*$) before barite precipitation. The 1:1 dashed line refers to 100% recovery. Data below the line indicate a low Ba recovery, which could be due to the loss of Ba as barite precipitation in the subsurface prior to venting or in the samplers.

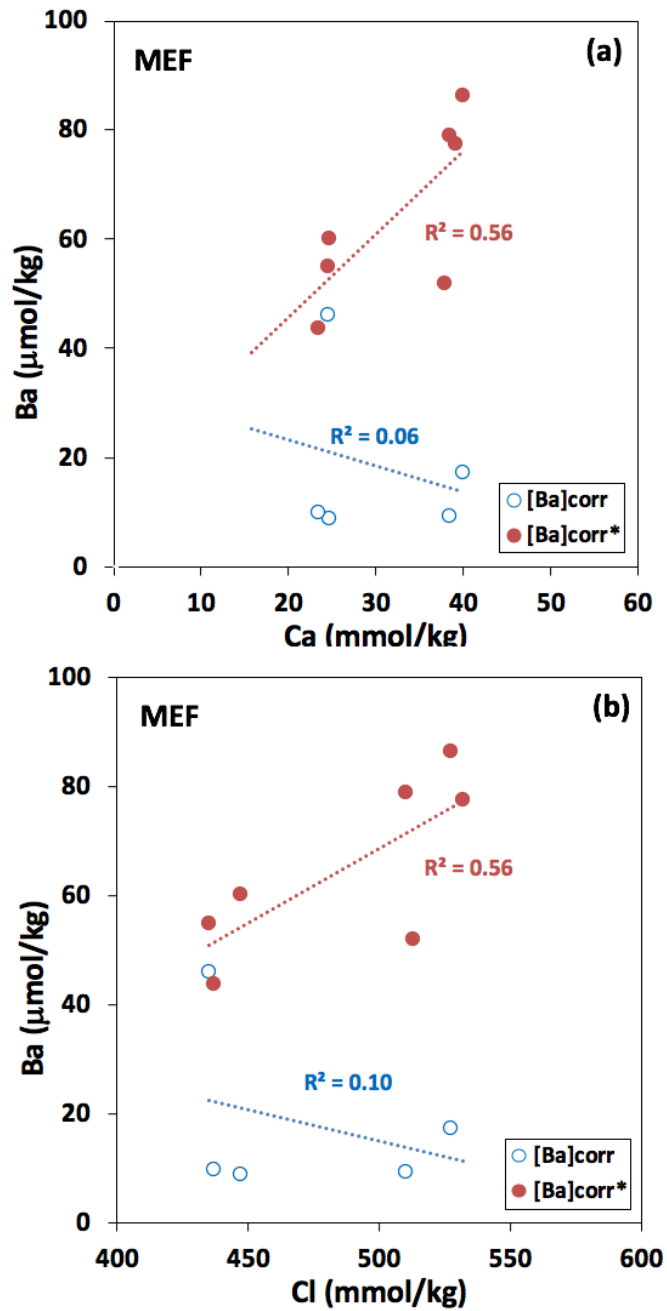


Figure S3. Comparisons of the corrected Ba concentrations between the dregs correction ($[\text{Ba}]_{\text{corr}}$) and the $\delta^{138/134}\text{Ba}$ -derived hypothetical Ba concentration ($[\text{Ba}]_{\text{corr}^*}$) prior to barite precipitation in the MEF vent fluids. The estimates of $[\text{Ba}]_{\text{corr}^*}$ values show a better correlation with (a) $[\text{Ca}]$ and (b) $[\text{Cl}]$ than the dregs corrected $[\text{Ba}]$, which may be a result of phase separation partitioning these species between the vapor and liquid phases.

Table S1 Vent fluids pH, Mg, Cl, Ca, SO₄, Ba and barite saturation index.

Vent	Type	Sample ID	pH (25°C)	Mg mmol/kg	Cl mmol/kg	Ca mmol/kg	SO ₄ mmol/kg	Ba			Ba Recovery		Ω_{barite} T=1°C; P=500bar ^a	
								$\mu\text{mol/kg}$ uncorr	$\mu\text{mol/kg}$ corr	corr*	(%) corr/corr*	uncorr	corr	
Rainbow (MAR 36°N) (2008) (36.23°N, 33.90°W)														
Guillaume, X4	FF	352-IGT4	3.31	2.8	756	67.9	0.66	56.7	97.9	96.9	101	7.0	12.2	
Regner	FF	353-IGT2	3.54	9.8	733	59.7	4.02	17.8	29.6	66.6	44	13.5	22.4	
CMSP&P	FF	354-IGT3	3.36	3.5	751	66.8	1.15	52.6	70.2	95.2	74	11.4	15.2	
Ecurie	DF	354-IGT4	5.05	33.8	631	34.1	17.2	4.54	26.2	20.0	131	14.7	85.1	
Ecurie	DF	354-IGT8	3.23	13.2	717	55.5	6.61	15.3	30.3	53.8	56	19.1	37.8	
TAG (MAR 26°N) (2008) (26.14°N, 44.83°W)														
TAG	FF	363-IGT5	3.63	3.9	632	39.4	2.0	9.22	24.0			3.5	9.1	
EPR9-10°N (2008) (9.83°N, 104.29°W)														
Bio-9	FF	4386-IGT6	3.23	1.9	313	13.9	1.1	3.78	10.5	8.9	118	0.8	2.2	
Tica	DF	4388-IGT5		29.3	366	9.94	16.0	0.89				2.7		
Ty-lo	FF	4393-IGT6	3.91	2.6	165	5.92	1.07	2.33	4.59			0.5	0.9	
Crab-Spa	DF	4394-IGT6	5.72	49.3	521	10.1	27.7	0.46				2.4		
Ty-lo	DF	4397-IGT5	6.52	51	533	10.0	27.7	0.43				2.2		
EPR9-10°N (2016) (9.83°N, 104.29°W)														
Bio-9	FF	4837-IGTD	3.35	1.8	285	9.58	0.7	13.9	14.1	15.2	93	1.8	1.9	
Bio-9	FF	4838-IGTB	3.13	1.6	268	9.97	0.8	6.27	6.44	6.5	99	0.9	1.0	
Pvent	FF	4838-2-6	3.67	0.9	313	11.0	0.8	7.47	7.64	9.3	82	1.1	1.2	
Pvent	FF	4841-2-4	3.47	1.4	324	11.2	0.9	7.92	8.08	8.7	93	1.3	1.4	
EPR13°N (2008) (12.83°N, 103.95°W)														
Grand Bonum	FF	4389-IGT5	3.34	2.2	642	44.2	1.1	8.02	13.4	13.4	100	1.7	2.8	
Dorian	DF	4391-MG		39.1	519	12.9	22.5	0.88				3.7		
Dorian	FF	4392-IGT5	3.49	2.3	466	21.2	1.1	6.17	10.2	17.1	59	1.3	2.1	
Jumeaux	DF	4392-MG		34.9	473	11.4	19.5	0.89		2.5		3.3		
Ph05	DF	4392-IGT6	5.78	41.8	552	11.8	23.7	0.72				3.2		
Actinoir	DF	4391-MW		47.3	528	10.7	26.5	1.51		1.5		7.5		
MEF (2014) (47.95°N, 129.10°W)														
Bastille	FF	4743-C	3.73	5.6	447	24.6	1.63	5.92	8.82	60.2	15	1.8	2.7	
Bastille	FF	4743-2	3.74	4.9	435	24.5	1.34	12.8	46.1	55.0	84	3.2	11.6	
Lobo	FF	4743-D	4.34	1.6	527	40.0	1.36	11.1	17.3	86.4	20	2.9	4.4	
TP	FF	4743-E	4.33	2.1	510	38.4	1.59	8.36	9.36	79.0	12	2.5	2.8	
Lobo	FF	4744-1	4.38	3.3	532	39.1	2.7	8.93		77.4		4.5		
Dante	FF	4744-2	4.43	2.2	513	37.8	1.91	9.72		51.9		3.5		
Sully Flange	DF	4743-4	5.62	29.4	497	15.8	16.7	1.65				5.2		
Puffer	FF	4743-5	3.72	4.5	437	23.4	1.14	8.32	9.82	43.7	22	1.8	2.1	
S and M	FF	4743-6	4.27	4.2	484	30.0	2.57	4.73	7.83			2.3	3.8	
ASHES (2014) (45.93°N, 130.01°W)														
Inferno	FF	4741-D	3.79	5	689	45.5	2.47	13.2	14.3			6.1	6.6	

^aBarite saturation model conditions and parameters: T=1°C; P=500 bar; LogK = -9.957; γ = 0.1442 (Monnin 1999).

*The $\delta^{138/134}\text{Ba}$ -derived hypothetical Ba concentrations in vent fluids prior to barite precipitation.